Investigating Charge Transport and Doping Effects of Reduced Graphene Oxide using Scanning Probe Microscopy Techniques

Christopher E. Kehayias

Contents

1. Introduction **3**
1.1 Overview of Graphene 3
1.2 Atomic Force Microscopy 6
1.2.1 Tapping Mode 6
1.2.2 Electrostatic Force Microscopy 8
1.2.3 Scanning Kelvin Probe Microscopy 9
1.3 Transistors 11
1.3.1 Field Effect Transistor Configuration 11
2. Experimental Procedures **13**
2.1 Preparation of Reduced Graphene Oxide Microassemblies 14
2.2 Transport Measurements 15
2.3 SKPM Potential Maps 17
2.4 EFM Charge Distributions 17
2.5 Scanning Impedance Microscopy Measurements 18
3. Results and Analysis **18**
3.1 Proof of Concept 18
3.2 Distribution of Charge 20
3.3 Shifts in Fermi Energy 29
3.4 EFM Measurements on RGO 29
3.5 SIM Measurements on RGO 30
4. Conclusions **32**
5. Future Developments **34**

Motivation

Graphene is rising as a promising candidate for nanoscale electronics due to its unique two-dimensional structure and its high electron mobility (1). Reduced graphene oxide is an electronically hybrid chemical derivative of graphene that can be controllably tuned from an insulator to a semiconductor material via reduction chemistry. Due to their chemical structure and large surface to volume ratio, reduced graphene oxide sensors can be constructed to detect gas adsorption at very low concentrations.

The purpose of this study is to investigate the electron transport mechanism throughout the reduced graphene oxide structure. This requires state-of-the-art techniques that have the capability to perform measurements on materials at the microscopic and nanoscopic levels.

The gas sensing properties of sensors fabricated using reduced graphene oxide are characterized using novel combined transport-Scanning Kelvin Probe Microscopy and transport-Electrostatic Force Microscopy measurements, as well as Scanning Impedance Microscopy in the presence of different gas analytes. Once the charge transport mechanism is understood using models derived from scanning probe microscopy-based measurements, it is possible to improve the sensing ability of this material, and to also discover the material's potential as a constituent for small-scale electronic devices.

1. Introduction

1.1 Overview of Graphene

Graphene is a material consisting of a single atomic layer of sp^2-hybridized carbon atoms (1). Graphene was hypothesized by physicists in 1962 to have very unique mechanical and electrical properties (2). These properties were verified experimentally by physicists Andre Geim and Konstantin Novoselov in 2004, and each received the 2010 Nobel Prize in Physics. Graphene can be prepared by the mechanical exfoliation of solid graphite, which is simply multiple atomic layers of carbon sheets held together by weak intermolecular interactions (2). Due to the characteristic hexagonal lattice structure of graphene (shown in Figure 1), electrons can travel through this material with great ease compared to other semiconductor devices (3). The structure also serves as an explanation for the immense tensile strength of graphene (5). Charge carrier mobility in graphene is much higher than in any other known semiconducting material, making it an ideal component for nanoscale electronics (3).

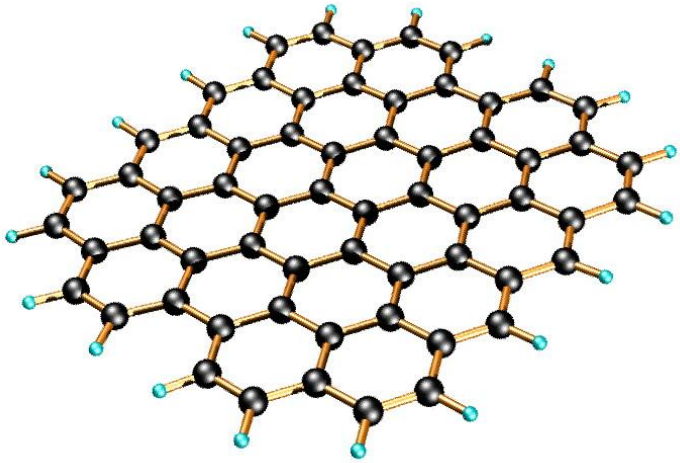

Figure 1: Graphene is depicted in the above ball and stick model as a sheet of sp^2-hybridized carbon atoms arranged in a hexagonal lattice (taken from http://www.ewels.info/img/science/graphite/)

The hexagonal lattice structure of graphene provides a unique potential for electrons residing within the material. One can compare this potential to the one constructed in the Kronig-Penney model. This model consists of a simple one-dimensional lattice of atoms. The electric potential created by such a lattice is therefore a superposition of Coulomb potentials, with singularities at each of the nodes of the lattice. Solving for the energy states of this quantum mechanical system yields results that are pictorially shown in Figure 2:

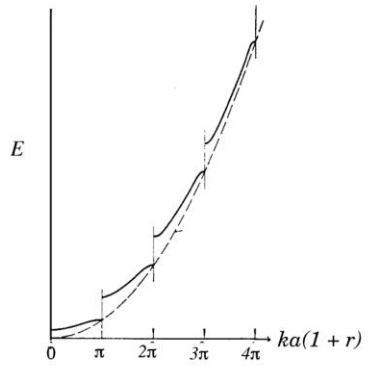

Figure 2: Energy solutions to the Kronig-Penney model as a function of wavenumber. Notice the discontinuities at each of the nodes (taken from http://web.alfredstate.edu/takeuchi/maple13.htm)

From the energy band diagram shown in Figure 2, we can surmise from the lack of overlap of the bands that if there were a hypothetical material that could be modeled with a Kronig-Penney potential, we would expect that this material would be semiconducting.

The model for graphene is similar, but it is two-dimensional and nearest nodes are every 120 degrees, not 180 degrees. The solution to the energy states, using a tight binding method, is shown is Figure 3.

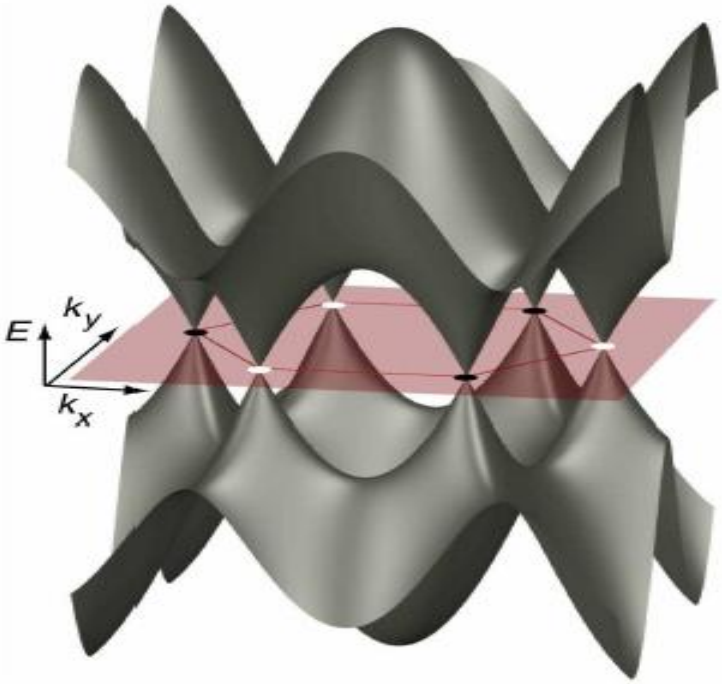

Figure 3: Above is shown the Energy diagram for graphene in reciprocal space. It is important to notice the continuities at the nodes of the energy diagram (taken from http://www.hindawi.com/isrn/cmp/2012/501686/fig3/).

This time, we can see that there exists a point continuity between the energy surfaces at each of the nodes. This is important because it means we can tune the material to be metallic or semiconducting by adding impurities or by changing the arrangement of the hexagonal lattice (to a zig-zag or arm-chair arrangement, for example). We will discuss later that this has key implications to the applications of graphene.

Another important result from the physical calculations of graphene is that, due to the unique potential it provides, the residing electrons can move through the material very easily. Charge carrier mobility measurements have been reported to be up to 15,000 $cm^2/ V \cdot s$, which is certainly much larger than the generally accepted value of 1,400 $cm^2/ V \cdot s$ for pure silicon, 2,320 $cm^2/ V \cdot s$ for copper, and even 4,840 $cm^2/ V \cdot s$ for gold (20). Thus, electrons can travel easily through graphene, making the material an ideal constituent for high-frequency electronic components (3).

The aim of this research project is to explore the chemical sensing properties of reduced graphene oxide (RGO). RGO is a chemical derivative of graphene that has been oxidized and partially reduced in order to introduce carboxyl and alcohol groups that act as binding sites for chemical sensing, while retaining some of the electrical characteristics of the original graphene (Figure 4 shows the physical structure of RGO). This material is ideal for sensing due to its characteristic two-dimensional structure, allowing for a very high surface-to-volume ratio. This ensures that the material is electrically sensitive to chemical doping, as each molecule that attaches itself to a binding site has a great impact on the material's conductivity, and also that the sensor has a quick response to doping.

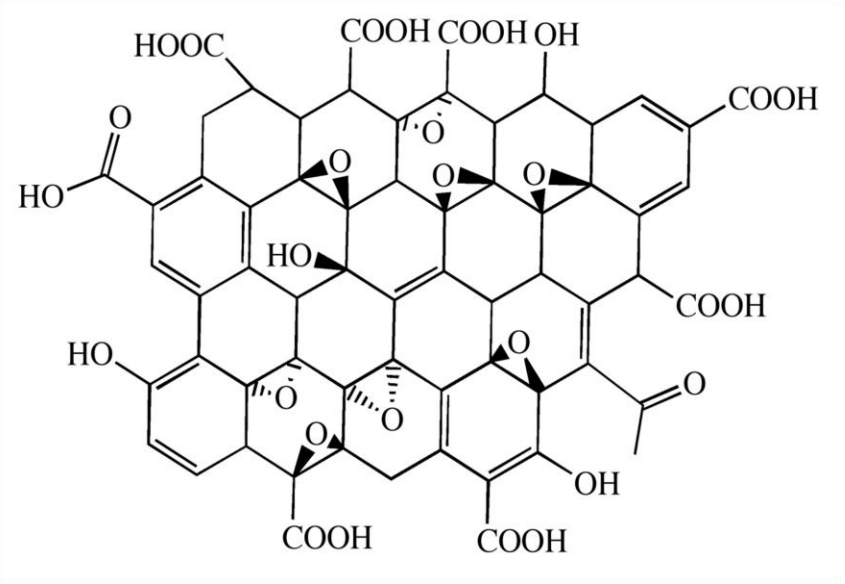

http://cnx.org/content/m29187/latest/

Figure 4: Shown is the physical structure of RGO. After being oxidized and partially reduced, RGO retains most of its former hexagonal lattice structure, but now has added oxygen, hydroxide and carboxyl groups that act as binding sites for chemical sensing.

1.2 Atomic Force Microscopy

AFM is a Scanning Probe Microscopy-based technique that is used for imaging and perturbing (mechanically, electrically, or otherwise) flat samples on the order of micrometers to nanometers. Topographical images are obtained by measuring the interaction force between a scanning probe (in our case, a cantilever) and the sample. Our cantilevers are fabricated with a fine conical tip (radius approximately 10 nm). The AFM rests above the sample, and so measurements are taken by lowering the cantilever down near the sample, thereby exposing the tip to the surface characteristics of the sample. If brought into contact, the resulting interaction between the tip and the surface is repulsive due to the Pauli exclusion principle. Otherwise, resulting repulsive interactions could include van der Waals forces, dipole-dipole interactions or electrostatic forces.

1.2.1 Tapping Mode

In tapping mode, the cantilever is driven to oscillate at near its resonant frequency using a piezoelectric device that is connected to the component of the AFM that houses the cantilever. The result is high amplitude of this oscillation, which is generally around 100 to 200 nm. The cantilever tip is brought closer and closer to the surface of the sample until it just begins to tap the surface, thereby reducing the energy of oscillation. This reduction in energy is monitored by measuring the deflection of a laser reflected off the top surface of the cantilever tip and directed into a sectioned photodiode. The reduction in oscillation amplitude is used to identify and measure features on the sample surface, thus making it possible to derive topographical scans using this method. Figure 5 displays a cantilever imaging a flat surface using this mode of operation.

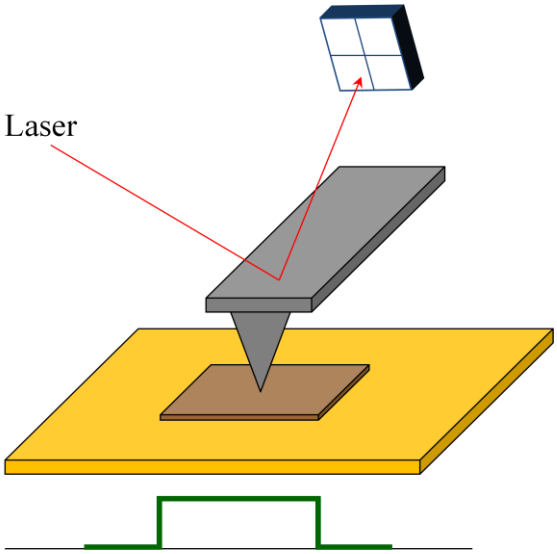

Figure 5: Diagram of a cantilever being used to scan the topography of a two-dimensional sample.

Figure 6 below shows a topographical image of a pair of gold electrodes with RGO deposited across the gap between them. This image was taken with an AFM.

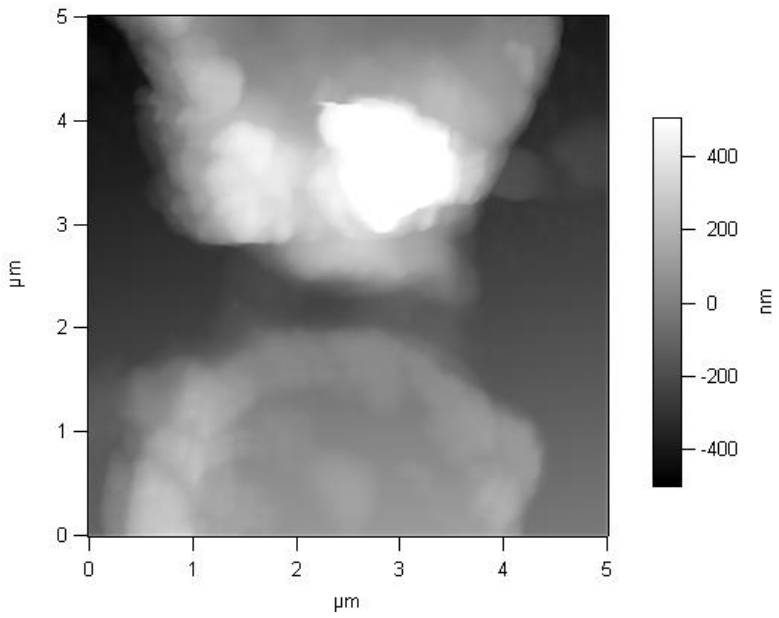

Figure 6: Topography map of RGO sensor. RGO platelets (center) are deposited between two gold electrodes (top and bottom).

1.2.2 Electrostatic Force Microscopy

Electrostatic Force Microscopy (EFM) is an extension of the Tapping Mode operation used in AFM. EFM is used to detect local charge distributions across a sample. In order to accomplish this, an electrical cantilever tip (coated with a layer of platinum over a layer of titanium over the silicon tip) is raised to a certain potential, thereby coupling the oscillations of the cantilever to the local surface charge of the sample. As Coulomb interactions are now responsible for the forces between the tip and the samples, the cantilever is raised a predetermined height above the sample between successive scans of topography in order to account for these long-ranged interactions (and also to eliminate short-ranged interactive forces such as van der Waals forces as a source of interaction). In more analytical terms, the potential applied on the tip provides a capacitance between the tip and the sample. The total energy stored within this capacitance is denoted by the expression is $U = \frac{1}{2} C \cdot \Delta V^2$, and the work done by the power source that is applying bias to the tip is $-2U$ in order to maintain a fixed bias between the tip and the sample. The resulting force is therefore a function of the negative gradient of the total energy ($U - 2U = -U$), and so the resulting force amounts to:

$$F_{electrostatic} = \frac{1}{2}\frac{\partial C}{\partial z}\Delta V^2 \tag{1}$$

We have that $\frac{\partial C}{\partial z}$ is always negative, and thus we are left with an attractive force. Analyzing the phase of this force is useful for determining charge distributions. The following derivations explain how this is.

We already have $F_{EFM} = \frac{1}{2}\frac{\partial C}{\partial z}\Delta V^2$ (Equation 1). Also, it is well known that $tan\theta \approx \theta$ for $|\theta| < 15°$. We also know the following is true for damped harmonic oscillators:

$$\ddot{z} + \gamma\dot{z} + {\omega_0}^2 z = \frac{F_0}{m}\cos(\omega t) - \frac{F}{m} \tag{2}$$

where z is the direction that determines the tip height above the sample (if the sample is perfectly flat and if we assume a perfectly conical tip, then we have achieved cylindrical symmetry). Rearranging this gives us

$$\ddot{z} + \gamma\dot{z} + \left({\omega_0}^2 z + \frac{F}{m}\right) = \frac{F_0}{m}\cos(\omega_0 t) \tag{3}$$

Finally, we employ the familiar relation for phase

$$\theta = \arctan\left(\frac{\omega\omega_0 \cdot \gamma/\sqrt{mk}}{\omega^2 - {\omega_0}^2}\right) \quad (4)$$

where *m* is the mass of the cantilever and *k* is the spring constant. We then have that the following is true,

$$tan\theta \approx \theta \approx \frac{Q}{2k}\left(\frac{d^2C}{dz^2}\right)\Delta V^2 \quad (5)$$

where *Q* is the quality factor of the cantilever. Therefore, we have shown that phase is proportional to the difference between surface and tip potential squared. Deviations from this model upon scanning a particular sample illuminate regions within the sample that have higher or lower concentration of charge, which makes EFM very useful for our purposes.

1.2.3 Scanning Kelvin Probe Microscopy

Scanning Kelvin Probe Microscopy (SKPM), like EFM, is another mode of operation that employs the technique of using an electrical cantilever scanning the topography of a particular sample and then retracing this sample in order to perform electrical measurements. SKPM, however, is used to map the surface potential of a sample instead of using phase of oscillations to infer charge concentrations.

SKPM is performed by employing the following technique. Typically, an AC signal is used to drive the oscillation of the cantilever when it is scanning topography. However, during SKPM measurements, this AC voltage is rerouted to the tip voltage, and there is no longer any driven oscillation of the cantilever, thereby allowing the cantilever to be oscillated only by the Coulomb interactions and the restoring force with spring constant of approximately 0.65 N/m to 1.0 N/m. A DC voltage is also applied to the cantilever tip, and this DC component is swept until the tip voltage matches the surface potential. This effectively minimizes the oscillation of the cantilever, as can be shown using the following derivation.

First, we have that the potential difference between the tip and the sample is described by

$$V = \left(V_{DC} - V_{sample}\right) + V_{AC}sin(\omega t) \quad (6)$$

where V_{DC} is the DC component of the tip voltage, V_{AC} is the amplitude of the AC component of the tip voltage, and ω is the resonant frequency of the cantilever. As was the case for EFM, the force can be expressed as a function of the negative gradient of this potential (per charge) using equation 1. For purposes that will become clear, it has been decided to express the force as a sum of three terms- namely, the constant for to DC components only, the force associated with the resonant frequency ω, and the force associated with twice the resonant

(7)

frequency 2ω (this results from trigonometric identities once the $V_{AC}sin(\omega t)$ term is squared, as required by equation 1).

$$F = F_{DC} + F(\omega) + F(2\omega)$$

Carrying out the operations described in equation 1 gives us the following:

$$F_{DC} = \frac{\partial C}{\partial z}\left[\frac{1}{2}\left(V_{DC} - V_{sample}\right)^2 + \frac{1}{4}{V_{AC}}^2\right] \quad (8)$$

$$F(\omega) = \frac{\partial C}{\partial z}\left[V_{DC} - V_{sample}\right]V_{AC}sin(\omega t) \quad (9)$$

$$F(2\omega) = -\frac{1}{4}\frac{\partial C}{\partial z}{V_{AC}}^2 cos(2\omega t) \quad (10)$$

The voltage applied to the tip causes three types of forces to exist between the surface and the cantilever (see equations 7 – 10), namely F_{DC}, $F(\omega)$, and $F(2\omega)$ (where ω is the natural frequency of the cantilever). Using lock-in detection, oscillations caused by $F(\omega)$ are analyzed. It is important to notice that the oscillations due to $F(\omega)$ are minimized when $V_{DC} = V_{sample}$, which means it is possible to sweep the DC component of the voltage on the tip until this force is minimized, thereby providing a means for matching the DC component of the voltage on the tip to the surface potential. A feedback loop detects this minimization and records this matching DC voltage for every point on the scanned region. Figure 7 shows a schematic of SKPM performed over a flat surface.

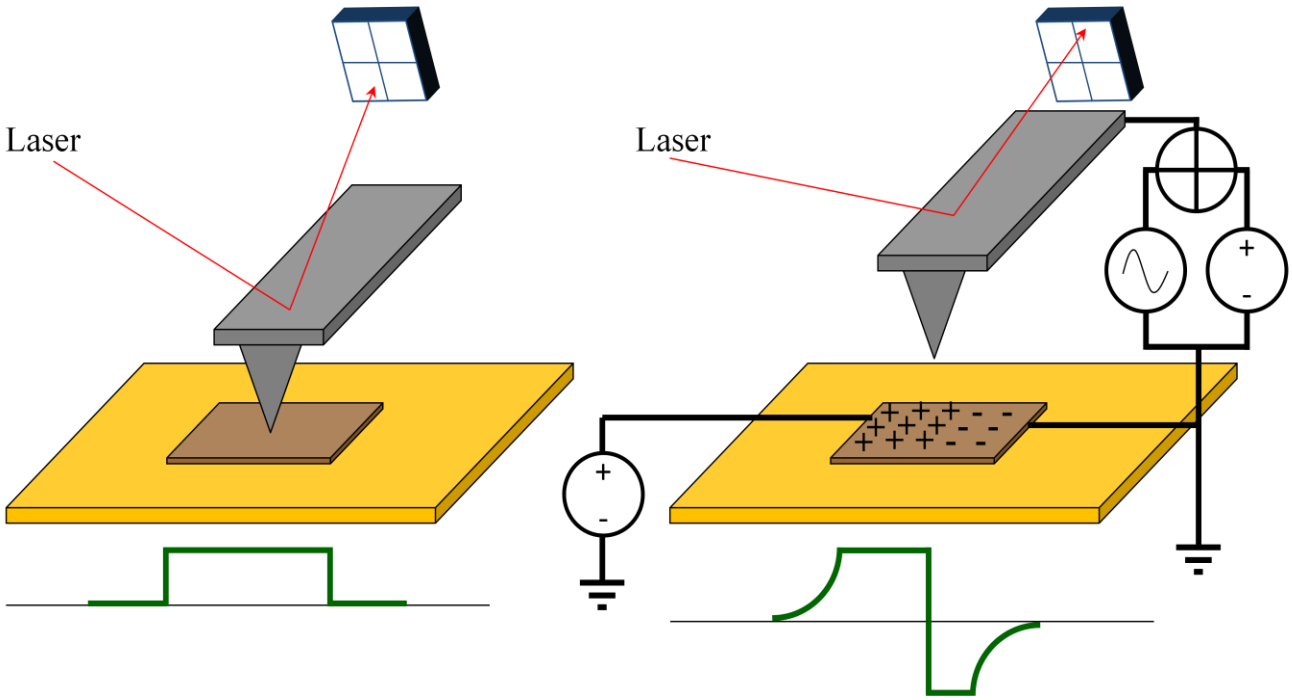

Figure 7: (a) During SKPM, topography is scanned first. (b) The surface potential is acquired by retracing the topography at a predetermined height above the sample and applying a voltage with an AC and DC component to the tip.

1.4 Transistors

Transistors are semiconductor devices with three terminals. One of these terminals allows for controlling the current flow between the other two terminals. As a result, it is common to describe a transistor as a type of electronic valve. Transistors are electronic components in nearly every electronic device used today, due to their ability to be used in integrated circuits (12, 13). A transistor can be used in circuits in order to control another transistor, which in turn can be used to control another transistor, and so on. This phenomenon provides the basis for constructing high-complexity circuits and microchips (14) For our purposes, however, we only employ the use of a single transistor-type configuration. There are two general types of configurations. The first is a Field Effect Transistor (FET) configuration, and the second is the Bipolar Junction Transistor (BJT) configuration. Our experiments are concerned with only the FET configuration.

1.4.1 Field Effect Transistor Configuration

The operation of a Field Effect Transistor is characterized as the control of a channel of majority-carrier flow using a voltage applied to a reverse-biased p-n junction (shown in

Figure 8), where p represents a p-type material (one with excess holes) and n represents an n-type material (one with excess electrons). This control voltage determines the width of the depletion region (the region where excess and holes annihilate each other at the junction), and therefore is used to control the width of the resulting channel that is produced by the electric field maintained by the control voltage.

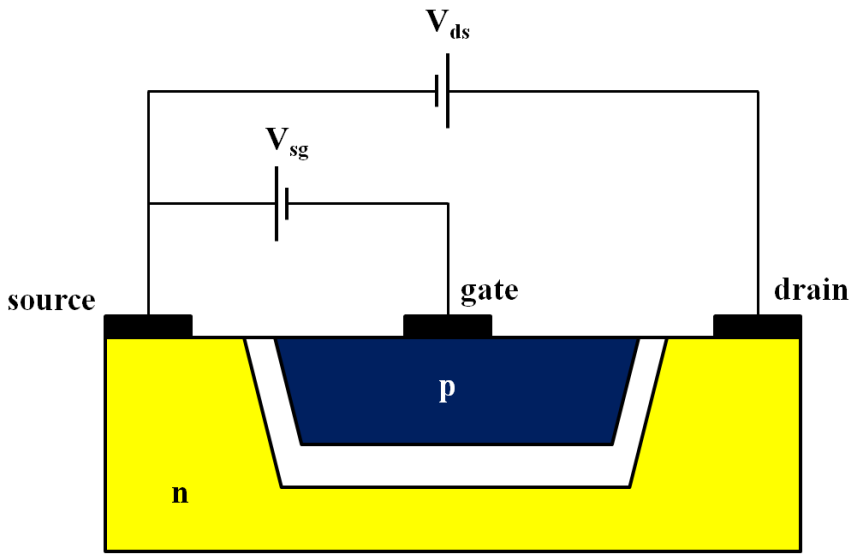

Figure 8: Shown is an n-channel junction field-effect transistor. The n-type material is shown in yellow and the p-type material is shown in blue. The depletion region is shown as the region in between in white. Majority carriers (in this case, electrons) flow from the source to the drain by means of a channel created through the semiconducting material by means of an electric field resulting from the reversed-biased gate terminal.

This FET configuration is precisely the one used for the RGO sensors in our experiments. In Figure 9, an array of pairs of gold electrodes (source and drain) is shown lithographically patterned on a 1 cm^2 Silicon wafer, with wire bonds connected to pins on the housing circuit board that serves as an extension of the three terminals.

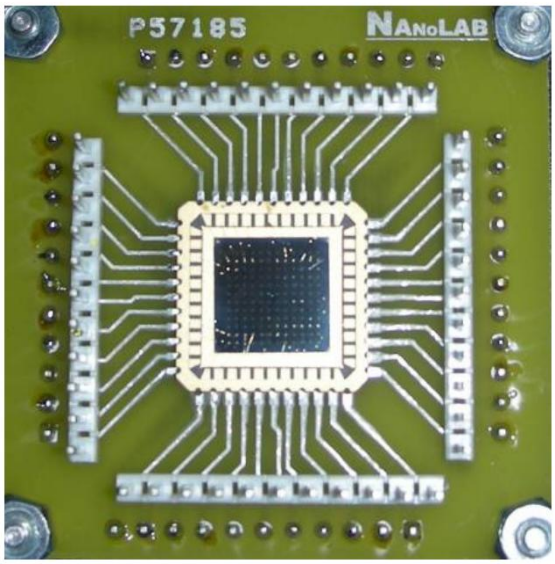

Figure 9: In the center, an array of pairs of gold electrodes is shown lithographically patterned on a 1 cm^2 Silicon wafer. Wire bonds connect these electrodes to pins on the housing circuit board for facile connections whilst performing experiments.

2. Experimental Procedures

The following experiments were used to verify that the sensors constructed from RGO assemblies display highly selective and reversible responses to certain measured analytes, as well as fast response and recovery times. We used combined electronic transport and Kelvin Probe Microscopy measurements to quantify the amount of charge transferred to RGO due to chemical doping when the device is exposed to electron-acceptor (acetone) and electron-donor (ammonia) analytes. We demonstrated that this method allows us to obtain high-resolution maps of the surface potential and local charge distribution both before and after chemical doping, to identify local gate-susceptible areas on the RGO surface, and to directly extract the contact resistance between the RGO and the metallic electrodes. Since the method presented is general, it is suggested that these results have important implications for fabricating graphene and other nanomaterial-based chemical sensors. We also measured localized charge distributions throughout the RGO surface with and without exposure to acetone vapor.

2.1 Preparation of Reduced Graphene Oxide Microassemblies

The RGO assemblies were fabricated using the following process. Graphene oxide was synthesized using the Hummers method (23), where graphite was treated with a certain mixture of sulfuric acid (H_2SO_4), sodium nitrate ($NaNO_3$), and potassium permanganate ($KMnO_4$). A typical procedure includes adding two grams of graphite nanoplatelets and one gram of $NaNO_3$ to 50 ml of concentrated H_2SO_4 (23). The mixture is stirred and then cooled to 0^oC, and six grams of solid $KMnO_4$ is added (23).After allowing the mixture to return to room temperature, the reaction vessel is then placed in a warm water bath where the temperature is maintained at approximately 35^oC for roughly 30 min. The resulting mixture is slowly diluted with DI water, and then treated with H_2O_2 to reduce any residual $KMnO_4$ and MnO_2 to colorless and soluble $MnSO_4$ (23). The GO powder (Figure 10a) is filtered and repeatedly centrifuged and washed with aqueous 1M HCl and DI water until the pH of the supernatant is around 7, at which point it is oven-dried. To reduce the GO, either hydrazine monohydrate or ascorbic acid (Vitamin C) is used as a reducing agent (Figure 10b). The reduction reaction is marked by the flocculation (producing of flakes) of RGO (23). The RGO is centrifuged and washed with 15 ml DI water and centrifuged five times (23). The RGO powder is added to 5ml of dimethyl formamide (DMF) containing 40 mg Triton-X100 non-ionic surfactant. A fine dispersion is obtained by probe sonication (Figure 10c). To create assembly sites for the carbon sensing elements, gold electrodes were patterned onto silicon wafers (Figure 11a) with 200 nm of thermal oxide using conventional lift-off photolithographic and sputtering metallization techniques (23). The distance between electrodes measured between 2 and 3 micrometers. RGO platelets were assembled between the electrodes by dielectrophoresis (Figure 11b) using the following procedure. First, the RGO dispersions were probe-sonicated for two minutes. A small drop of the desired dispersion was placed with a syringe on the chip, covering the assembly site (23). A function generator was used to supply the voltage signal necessary for dielectrophoresis. RGO was assembled using a signal with frequency range 50kHz to 500kHz, with peak-to-peak amplitude of around 10V. After approximately five minutes of assembly, the drop of suspended RGO was blown off using compressed dry air (Figure 11c).

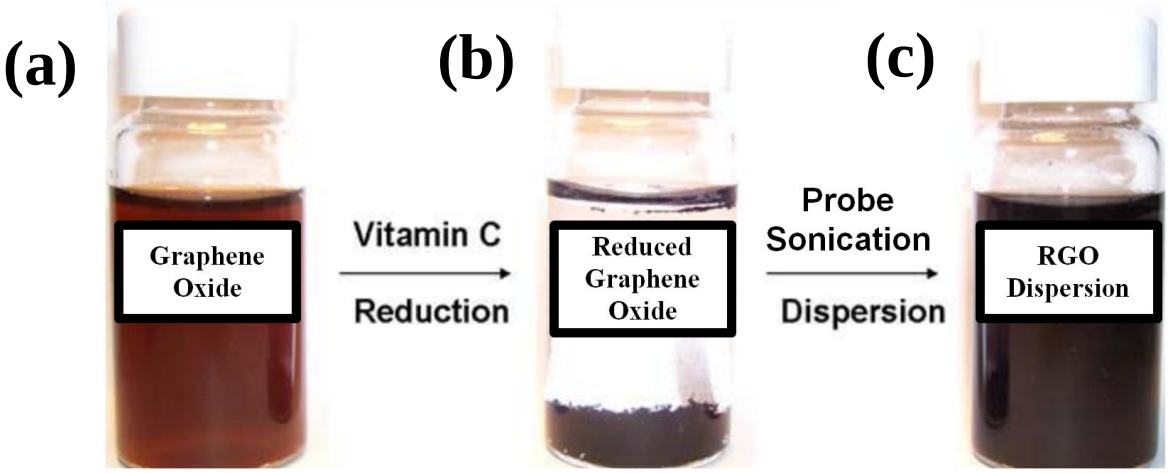

Figure 10: (a) GO is prepared using the Hummers method (23). (b) Using Vitamin C reduction, RGO flakes are produced. (c) Probe sonication is performed on the RGO mixture to create a fine dispersion (Image taken and edited from Samuel Macnaughton et. al. p. 895, 2010. IEEE SENSORS 2010 Conference).

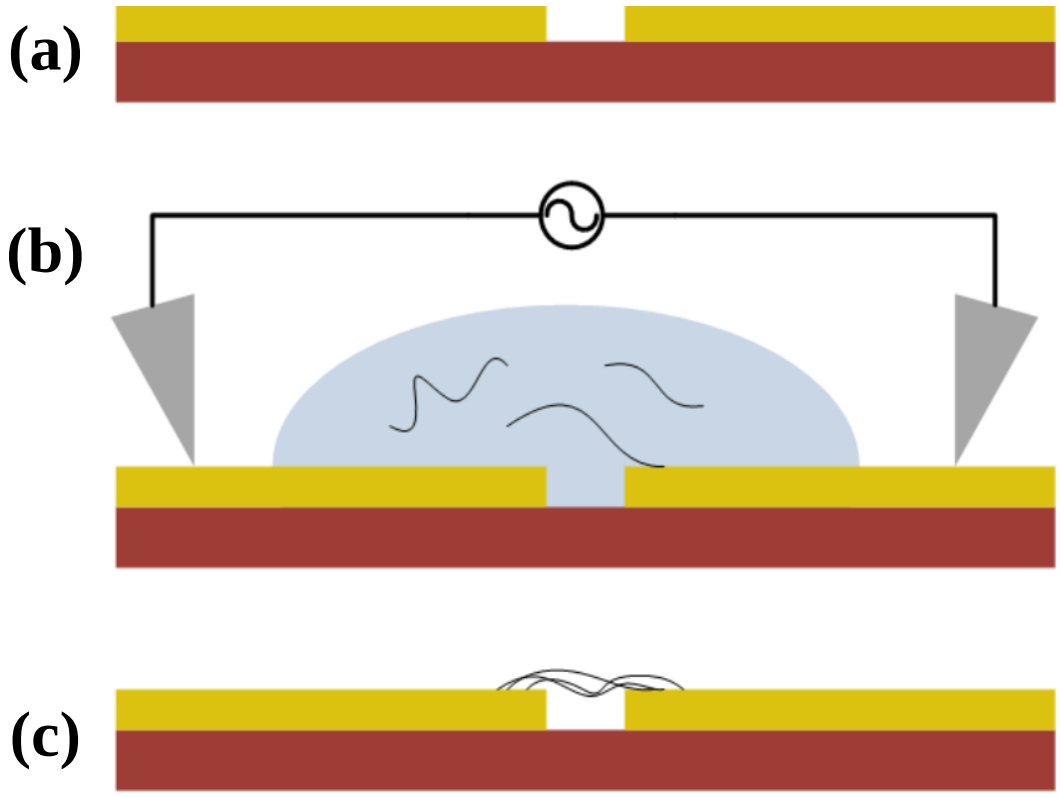

Figure 11: (a) Gold electrodes are patterned on a SiO_2 layer. (b) RGO platelets are assembled across the electrodes using dielectrophoresis. (c) The remaining solution is blown off using compressed dry air (Image taken and edited from Samuel Macnaughton et. al. p. 895, 2010. IEEE SENSORS 2010 Conference).

After RGO platelets were patterned across gold electrodes using dielectrophoresis, wire bonds were used to connect the source and drain terminals of each sensor site to an external circuit board. The gate terminal was constructed by applying conductive paste to one side of the silicon wafer, ensuring conductivity between the silicon substrate and one of the pins on the circuit board (Figure 12 shows this configuration).

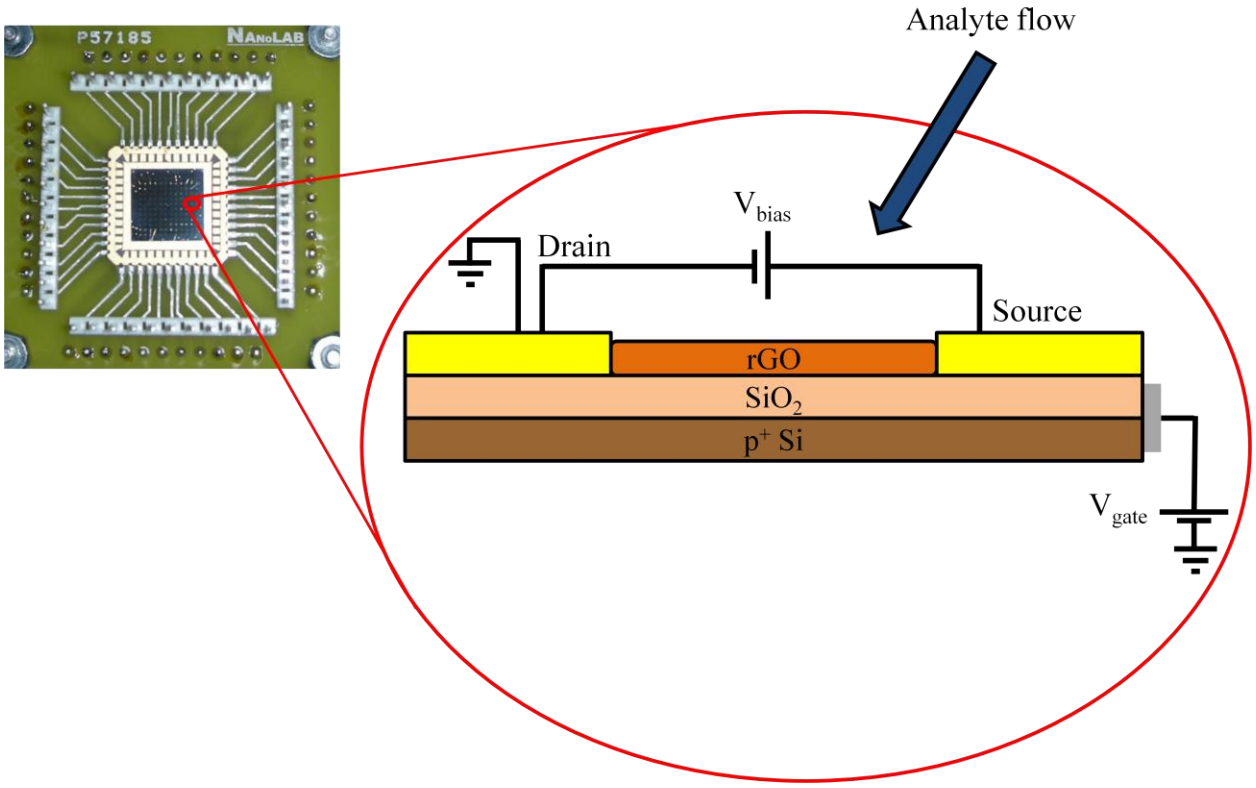

Figure 12: Shown in the upper left is the circuit constructed as described in Figure 9. The red outline shows a zoomed-in vertical cross-section of one of the RGO assemblies. This is a standard FET configuration, showing a forward bias applied across the source and drain terminals. The drain terminal is connected to common ground, while a positive bias (V_{bias}) is applied across the source and the drain. A voltage is applied to the gate terminal, shown on the right side of the FET schematic. Analyte flow occurs above the region where the RGO platelets have been deposited.

2.2 Transport Measurements

The gas sensing properties of these devices were first demonstrated and characterized using electrical transport measurements in the presence of gas analytes (see Figure 12). We have used a sample (source-drain) bias voltage of 1V (DC), and V_{gate} = 0V for these measurements. Acetone and ammonia vapors were delivered to the device from a reservoir of saturated vapors through a peristaltic pump. The vapors used were highly concentrated (as

concentrated as was allowed at room temperature and pressure), so as to maximize the response of each sensor. Figure 13 serves as a demonstration for the responsiveness of the RGO sensors when exposed to different organic vapors, performed by Samuel MacNaughton and Professor Sameer Sonkusale (the manufacturers of these RGO samples) from Tufts University Electrical Engineering department.

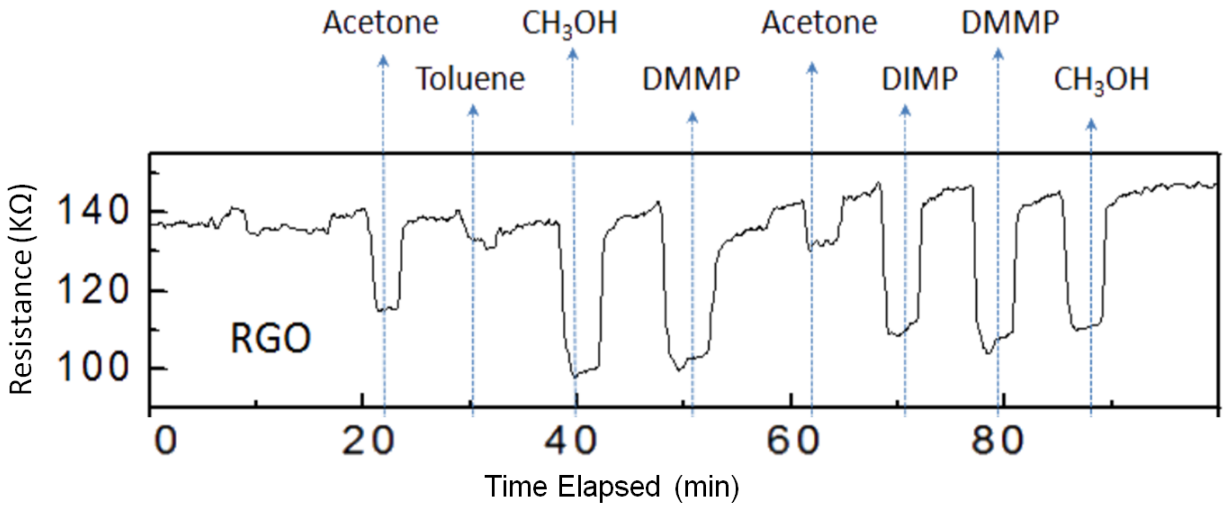

Figure 13: Shown above is a resistance versus time depiction of an RGO sensor while exposed to various organic dopants. Each blue arrow indicates when a dopant was introduced, and within a few minutes of each exposure, the dopant was removed from the system (Image taken from Samuel Macnaughton et. al. p. 897, 2010. IEEE SENSORS 2010 Conference).

As is clear from the above figure, the conductivity of the RGO system varies dramatically when exposed to certain dopants. Similar resistance versus time curves are shown in Figure 14, performed in our laboratory at Tufts University Science and Technology Center.

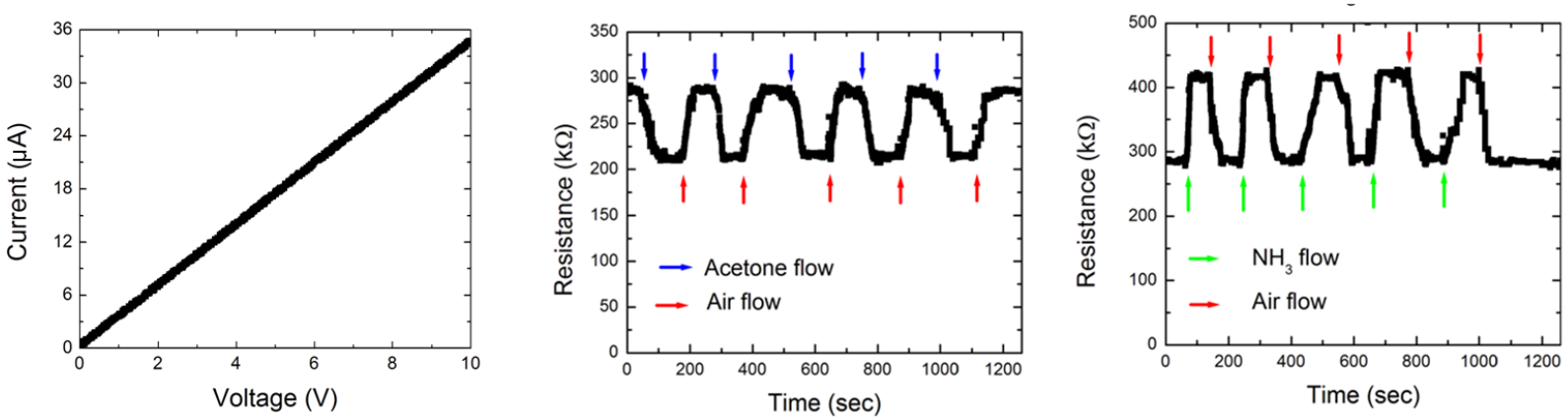

Figure 14: (a) The sensor demonstrates linear relationship between voltage and current with zero gate bias, which means we can relate the response of the sensor due to exposure to different analytes purely in terms of resistance. (b) Acetone and (c) ammonia are introduced to a similar RGO sensor as the one used in the demonstration in Figure 13. Again, the analytes were introduced periodically, and then periodically removed from the system (indicated by red arrows).

Several transport experiments were performed on the RGO sensors. A Model 2400 Keithley sourcemeter was used to provide a steady 1V bias across the electrodes containing these sensors, while acetone (and later ammonia) was periodically introduced to the samples. Current was recorded as a function of time, marking the difference in resistivity when the sample was doped and undoped. From the collected data, variations in resistivity with respect to each type of analyte were calculated. Also, the sensitivity, specificity, and reproducibility (as well as excitation and relaxation time) for these RGO sensors were characterized from these transport measurements.

These measurements initially performed with zero bias voltage. However, similar types of transport measurements were taken with a wide range of gate voltages. These gate measurements aided in determining the underlying transport mechanism of the RGO system, as will be discussed in the next section, *Results and Analysis*.

2.3 SKPM Potential Maps

Next, charge distribution measurements were taken using SKPM to map the surface potential of nanosensor sites before and after exposure to acetone. As was discussed before,

the purpose of SKPM is to match the DC component of the cantilever potential to that of the surface. By doing this for each point on the scan, the SKPM images recorded the distribution of the surface potential along the sample surface. It is expected that, for the RGO surface, the following relation holds:

$$e \cdot \Phi(x, y) = W_{cn} - E_F \quad (11)$$

where e is the electron charge, W_{cn} is the work function (which is expected to be constant), and E_F is the Fermi energy. It was discovered in the literature that similar relations were demonstrated to hold for SKPM measurements on graphene (28). In our experiment, we used the aforementioned platinum and titanium coated electrical tips with curvature radius of approximately 20 nm, quality factor of 150, and spring constant of 0.65 – 1.0 N/m. The AC signal applied to the tip was 5V in amplitude and the SKPM scan height was h = 50 nm. The acquired potential maps were analyzed to measure variations in charge distribution, thereby illuminating the mechanism and extent of charge transfer due to chemical doping.

2.4 EFM Charge Distributions

EFM measurements were also performed on the same RGO sensors as with the SKPM measurements. From these measurements, phase maps were used to identify regions within the RGO platelets that had the largest increase or decrease in charge concentration, thus allowing for the determination of regions that were most susceptible to analyte exposure. These regions were hypothesized to be the locations of binding sites within the material.

The parameters of the EFM measurements used in this stage of experimentation were the following. The DC tip bias was set to 5V, and the EFM scan height was set to h = 70 nm. This latter value was obtained through repeated measurements in order to reduce the noise and optimize the resolution of the scan.

2.5 Scanning Impedance Microscopy Measurements

Finally, Scanning Impedance Microscopy was employed in order to experiment with high-resolution techniques on the same RGO sensors. With similar motivation to use this technique as with EFM, Scanning Impedance Microscopy (SIM) measurements were performed with the expectation that the analysis method could be extended to study local chemical gating effects within smaller gate-susceptible regions of the RGO sample, and to correlate the local surface charge with surface functional groups on RGO. The goal was to utilize SIM in order to investigate whether or not this technique can provide us with higher resolution images and possibly even illuminate the locations of active sites within the

molecular structure of the RGO samples. SIM is a novel Scanning Probe Microscopy (SPM) technique that utilizes the detection of the phase change of cantilever oscillations induced by an AC bias applied to the sample (Figure 12a). This bias induces oscillations in surface potential, thereby exerting a periodic force acting on the DC-biased tip. The lock-in component detects phase and amplitude of tip vibration. The phase and amplitude of the cantilever oscillation is recorded as SIM phase and amplitude images. The phase of the surface potential oscillations is related to the local transport properties of the sample. Thus, the variation of measured cantilever oscillation phase is equal to voltage phase angle variation across the surface. We tested SIM on one of our samples, with and without exposure to acetone, thus experimenting with this technique in a similar fashion to the other techniques we have utilized.

3. Results and Analysis

3.1 Proof of Concept

We have performed both transport (Figure 15b) and SKPM measurements (Figure 16) on several different RGO circuits, in air and in the presence of chemical dopants. Here we focus on the response of these sensors to acetone. The first of these sensors was analyzed in order to demonstrate the proof of concept. An AFM topography image of this first RGO sensor is shown in Figure 15a.

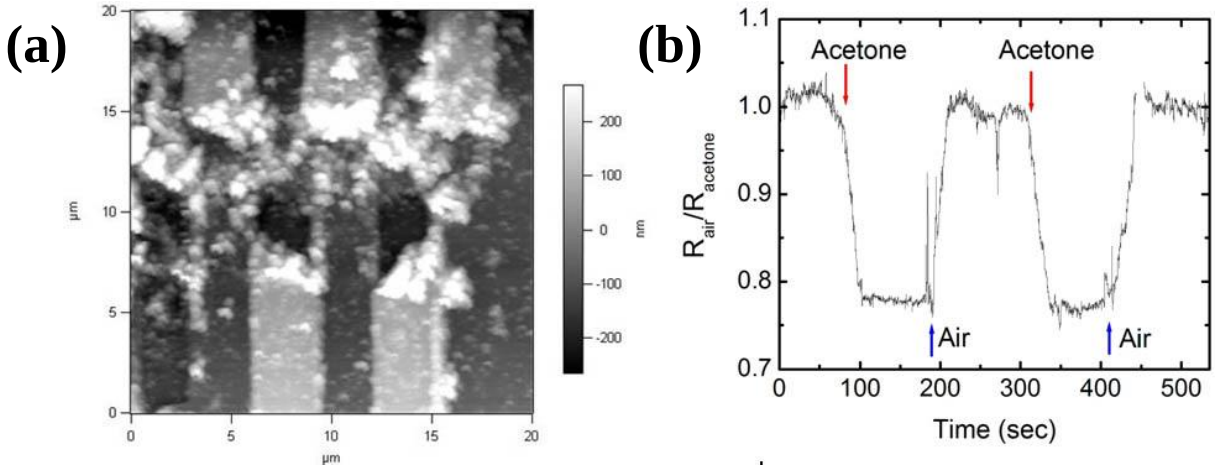

Figure 15: (a) AFM image of an rGO sensor circuit. The rGO platelets are assembled between Au electrodes (bright features in the image) using dielectrophoresis. (b) Typical

response of the rGO sensor to acetone. The air resistance was about 200 KΩ, and it decreased by about 25% upon exposure to acetone.

A total of 5 gold electrodes are seen in the Figure 15a (3 electrodes on top, and 2 on the bottom). Figure 15a also shows RGO platelets deposited between the electrodes. The typical height of a platelet is 100-160 nm, with a lateral dimension of approximately 0.5 µm. Figure 15b shows the dynamic response of this device to acetone, where $R_{air}/R_{acetone}$ is plotted vs. time (R_{air} and $R_{acetone}$ are the device resistances when exposed to air and acetone respectively). The value for the sensor air resistance was 200 KΩ, and upon exposure to acetone this resistance decreased by about 25% as shown in Figure 15b. This is consistent with previous reports found in literature (21). We also note that decrease in the rGO sensor resistance was also reported in literature for rGO exposure to chemical dopants similar to acetone (such as NO_2, methanol, dimethyl methylphosphonate etc.) (23, 32, 33).

We performed SKPM over both large (20 μm^2) and small (5 μm^2) areas of the rGO circuit, shown in Figure 16. The small areas (Figure 16b and Figure 16c) are selected to include only rGO platelets between the electrodes, That is, the Au electrodes are excluded from the scan. Thus we can directly compare the response from the same regions of rGO before and during exposure to acetone. A typical example is shown in Figure 16b and Figure 16c.

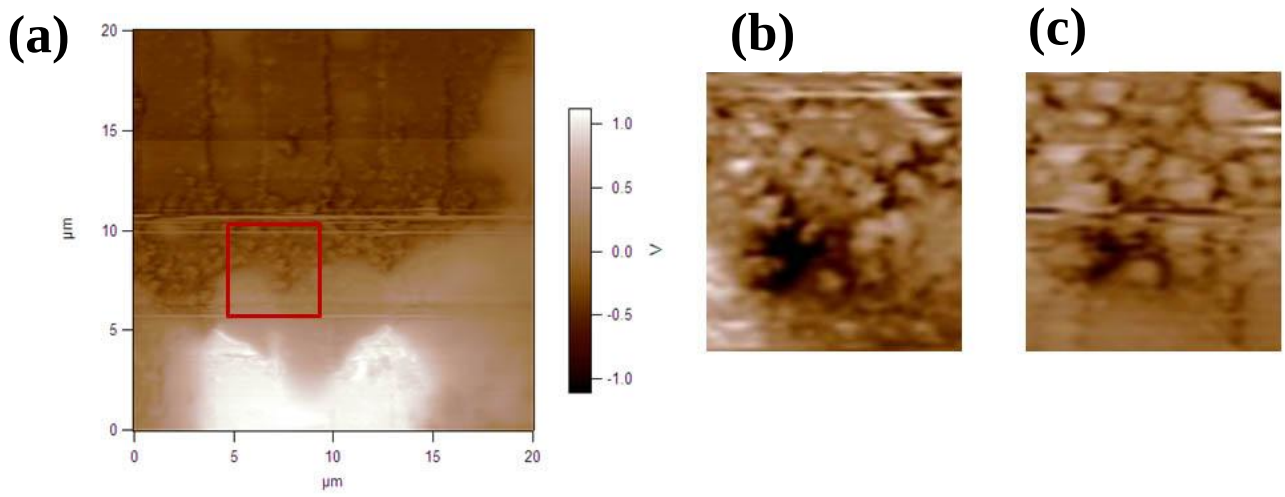

Figure 16: SKPM images of a typical RGO sensor circuit. (a) SKPM scan taken over a large area (20 μm^2) that includes the Au electrodes. The image was acquired in air, before exposure to acetone. The red square marks the areas used for measurements shown in the next images. (b) SKPM image of the area marked by the red square in (a) taken before exposure to acetone. (c) SKPM image of the same region shown in (b) taken while the sample is exposed to acetone (saturated vapors).

Figure 16b shows an SKPM image of an rGO region between electrodes taken with the sample exposed to air. Figure 16c shows the corresponding SKPM image of the same region taken while the sample is exposed to acetone. By analyzing the two images we find a definite shift in the surface potential, as measured by SKPM, due to sample exposure to acetone, was approximately 50 mV. Using the relation $e \cdot \Phi(x, y) = W_{cn} - E_F$, we discover that this is equivalent to a carrier Fermi energy of 50 meV. We also find that this shift is reversible upon re-exposing the sample to air.

3.2 Distribution of Charge

The miniaturization of the RGO sensors allows for facile integration with CMOS, so it is therefore possible to perform gated measurements of each sample. Figure 7b shows the variation of the source-drain current I_{SD} with the gate voltage V_G, for an RGO-FET device exposed to the following: dry air (shown in red), acetone (shown in blue) and NH_3 (shown in green). The source-drain bias voltage was V_B = 1V for each measurement. The device demonstrates principally p-type semiconducting behavior over the whole range of applied gate voltages (from V_G = -40V to V_G = +40V).

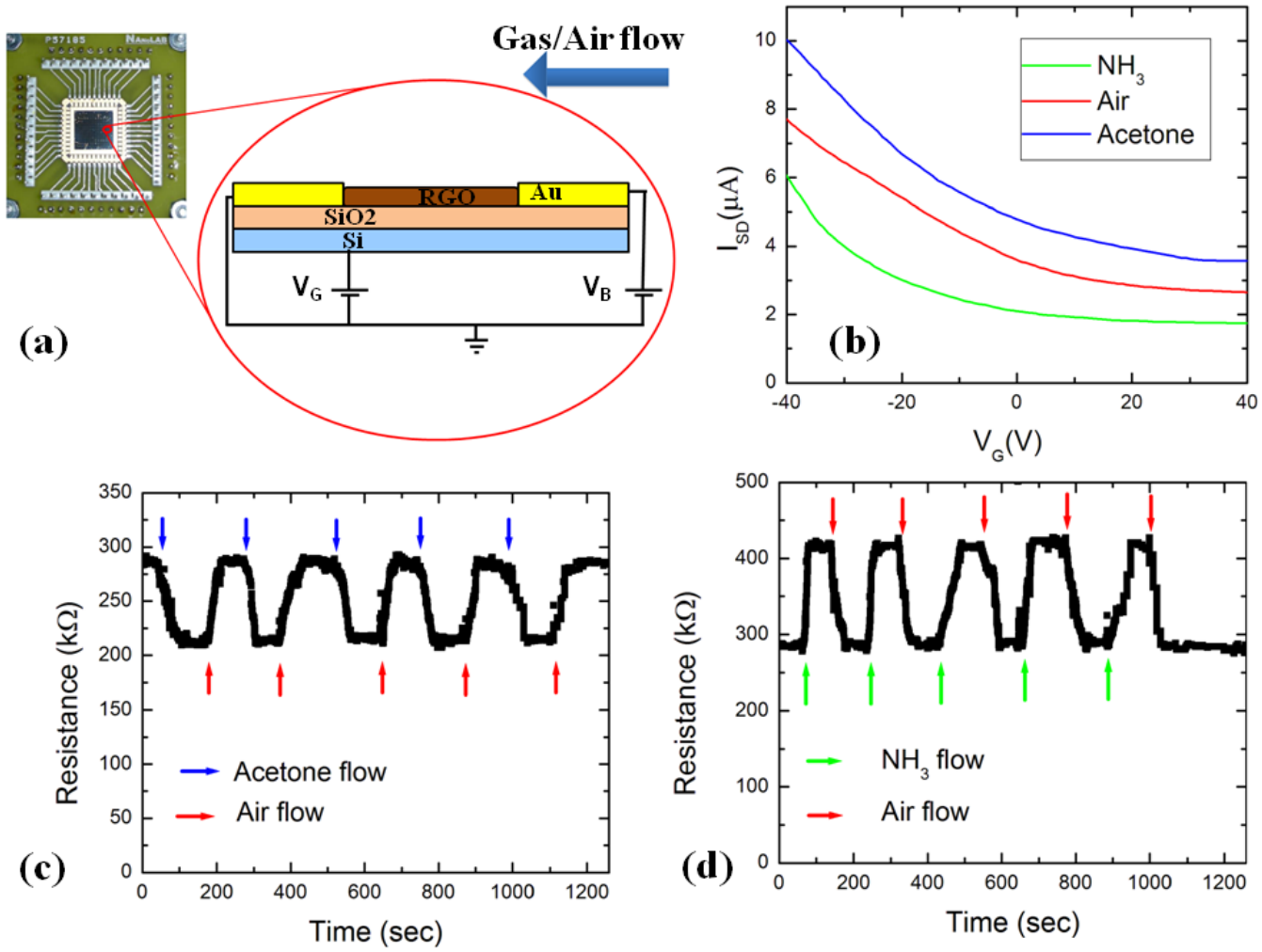

Figure 17: (a) Schematics of the electronic transport and gas sensing setup, identical to that of Figure 12. The RGO-sensing devices are patterned on SiO_2/Si wafer in a field-effect transistor configuration. V_B denotes the bias voltage and V_G denotes the gate voltage. RGO platelets are deposited between Au electrodes and aligned using dielectrophoresis. Each sensing device can be successively exposed to dry air and analytes (acetone and ammonia at a concentration of 200 ppm). (b) Source-drain current I_{SD} versus gate voltage V_G for a device while continuously exposed to: dry air (red curve), acetone (blue curve) and ammonia (green curve). The applied bias voltage was V_B=1V, and all gate sweeps were performed from -40V to +40V at a rate of 0.5V/sec. The device shows p-type response in air and the response to the analytes is characteristic for a chemical gating mechanism. (c) Dynamic response (device resistance versus time) for the device measured in (b), when exposed successively to dry air (red arrows) and acetone (blue arrows). 5 cycles are shown demonstrating reversibility and fast response and recovery times (tens of seconds). The decrease in device resistance upon acetone exposure is about 25%. (d) Dynamic response for the device measured in (b) and (c), when exposed successively to dry air (red arrows) and ammonia (green arrows). 5 cycles are shown demonstrating reversibility and fast response and recovery times (tens of seconds). The increase in device resistance upon exposure to ammonia is about 45%. The applied bias voltage was V_B=1V and the gate voltage was V_G = 0V for both (c) and (d).

The observed p-type behavior is consistent with previous results on RGO and graphene circuits obtained by chemical and thermal reduction of graphene oxide. The threshold voltage of the device, when exposed to air is $V_{th}^{air} = 23\text{V}$. This occurs when the minimum gate voltage at which I_{SD} is invariant with respect to V_G. When the device is exposed to acetone (which is an electron-withdrawing analyte) the source-drain current increases over the applied V_G scan range and the threshold voltage shifts to a larger value: $V_{th}^{acetone} = 28\text{V}$ (shown in blue in Figure 17b). When the same sensor site is exposed to NH_3 (an electron-donor analyte) we observe a decrease in I_{SD} and a shift in the threshold voltage towards smaller values: $V_{th}^{NH3} = 16\text{V}$ (shown in green in Figure 17b). These results demonstrate a charge transfer mechanism between the analyte (acetone or ammonia) and the RGO-FET sensor, where hole conduction dominates over electron conduction. NH_3 acts as an electron donor upon adsorption onto RGO, and it is expected to lower the concentration of charge carriers (holes), therefore decreasing the on-state current and shifting the threshold voltage towards the negative regime. Acetone serves as electron acceptor, and it is therefore expected to increase the charge carrier concentration, which results in increased on-state currents and threshold voltages. Similar chemical doping mechanisms have been proposed for graphene and RGO based sensors prior to these experiments (12-15, 24, 25).

The shifts of the I_{SD}-V_G transport curves in Figure 17 can be used to calculate the relative change in the density of charge carriers for acetone (Δn_a) and NH_3 ($|\Delta n_{NH3}|$) doping. Using $e \cdot \Delta n = C \cdot \Delta V_{th}$, where e is the electron charge, Δn is the variation in the number of charge carriers, C is the silicon dioxide layer gate capacitance and ΔV_{th} is the shift of the threshold voltage when the device is exposed to the analyte, measured relative to the threshold voltage when the device is exposed to air, we obtain:

$$\frac{\Delta n_a}{|\Delta n_{NH3}|} = \frac{V_{th}^{acetone} - V_{th}^{air}}{V_{th}^{air} - V_{th}^{NH3}} \approx 0.7 \qquad (12)$$

In Figure 17c and Figure 17d, we show the dynamic response (measured resistance versus time) for the RGO-FET sensor when exposed to analytes (acetone in Figure 17c, and NH_3 in Figure 17d). The resistance of the sensor was measured for V_B= 1V and V_G= 0V in air. The device was then periodically exposed to acetone or ammonia, and then air. The duration of each exposure (air or analyte) was about 100 sec. Five complete exposure cycles are displayed in Figure 17c and Figure 17d to demonstrate the reproducibility, stability, and effectiveness of the sensing ability of the RGO device. Once exposed to acetone, the sensor resistance decreased by about 25% (Figure 17c), while the device was exposed to NH_3 its resistance increased by about 45% (Figure 17d). The direction of the dynamic response is again consistent with the expected chemical gating response for the electron-withdrawing acetone and the electron-donor NH_3 vapors, which leads to a decrease in the concentration of charge carriers in the p-type RGO device. Figure 17c and Figure 17d also demonstrate that the sensor response to the analytes and its recovery upon air exposure are rapid (tens of

seconds) and reversible for the relatively low analyte vapor concentrations (200 ppm). The sensing characteristics (response and recovery times, sensitivity, and stability of the sensor) for these devices is at the level of the performance for graphene-based sensors reported in literature (12).

To gain a deeper quantitative understanding of the sensing mechanism, Kelvin Probe Microscopy (KPM) measurements were performed on RGO devices both in air and during exposure to acetone and NH_3. KPM measurements were performed over the RGO regions between the two electrodes (shown topographically in Figure 6), with the sample exposed to air (Figure 18a), acetone (Figure 18b) and then again to air (Figure 18c). This sequence corresponds to a complete exposure cycle shown in transport data (Figure 18c). The corresponding distributions in the surface potential are shown respectively in Figure 18d, e and f. The KPM data shows a clear shift in the average distribution of the surface potential upon exposure to acetone from V_{air}=173±33 mV (Figure 18d) to $V_{acetone}$= 242±38 mV (Figure 18e). After exposure to acetone the sample is exposed again to air and the average of the surface potential distribution V_{air}=176±25 mV approaches the initial average of the distribution.

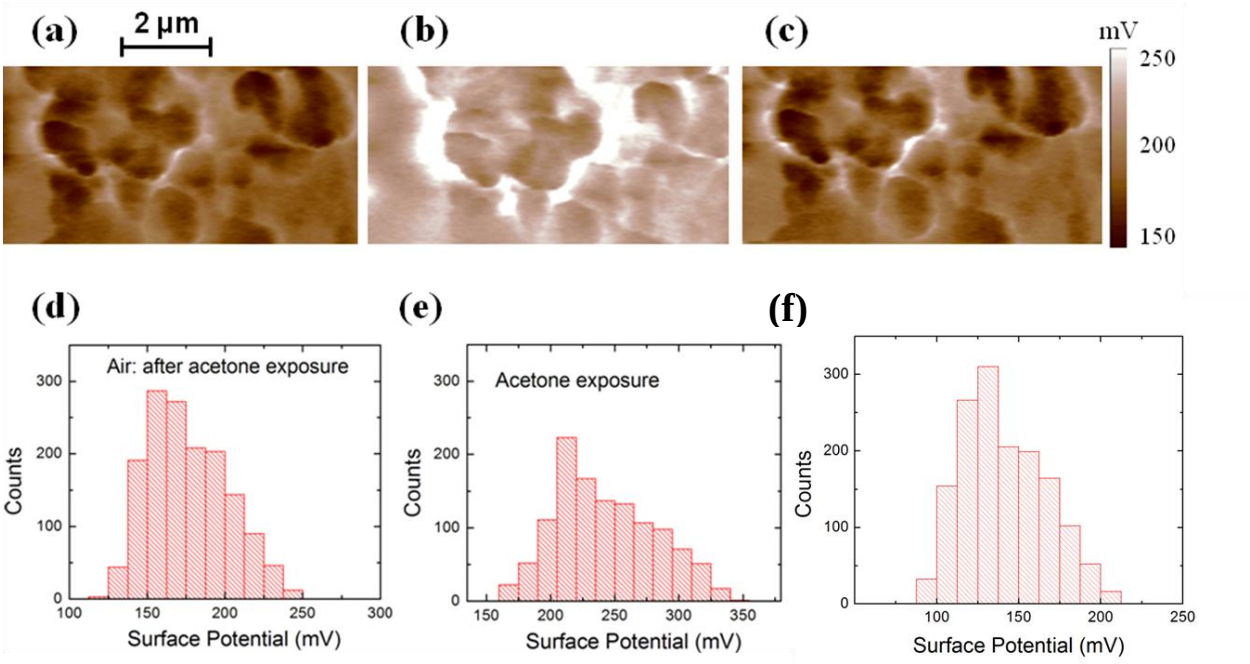

Figure 18: (a) SKPM potential map of nanosensor when it is unexposed. (b) SKPM potential map of nanosensor when it is exposed to acetone vapor. (c) SKPM potential map of nanosensor when it has had 30 minutes to relax since exposure to acetone. (d) Histogram of surface potential when unexposed with average value 178 mV and standard deviation 33 mV. (e) Histogram of surface potential when exposed to acetone with average value 243 mV and standard deviation 39 mV. (f) Histogram of surface potential when exposed to acetone with average value 131 mV and standard deviation 35 mV The difference in charge distribution throughout the sample is shown graphically in (a,b,c) and also numerically in (d,e,f), demonstrating the sensitivity of the nanosensors' response to acetone exposure.

The chemical doping model implies that the observed shifts in the surface potential are due to charge transfer between acetone and the sample. The theory is that vapor molecules of acetone adsorb near the sample surface, thus changing the electrostatic environment and increasing the concentration of hole charge carriers, thereby leading to an increased surface potential as measured by KPM. The KPM maps have high spatial resolution and thus allow for the identification of regions within the sample where the chemical doping effect takes place, as well as the local variations in the surface potential due to charge transfer between acetone and the RGO sample. This is confirmed by the comparison between Figure 9a and 9b, which shows that the chemical doping is not uniform along the RGO surface. It is also possible to discover regions where changes in surface potential is maximum upon doping, allowing for the identification of gate-susceptible regions on the sensor surface.

To further this analysis, similar types of measurements were acquired for yet another RGO sensor. Figure 19 shows the topography of this new RGO sensor site, while Figure 20 displays the results of SKPM measurements of this sensor before, during, and after exposure to acetone vapor.

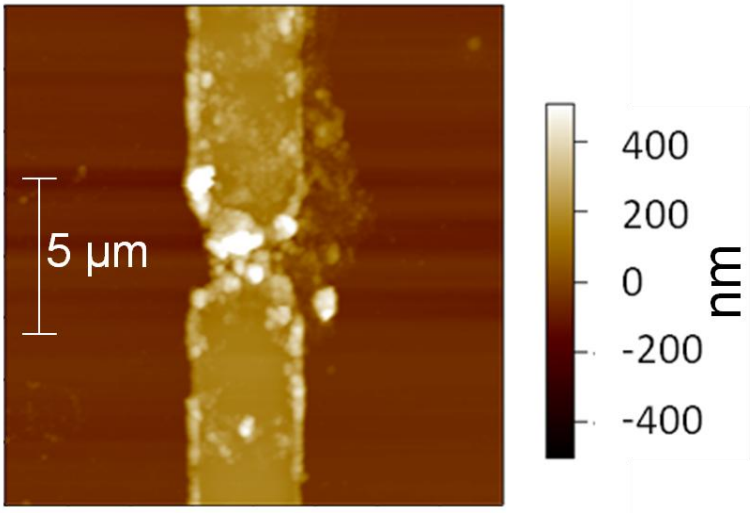

Figure 19: Shown above is a topographical AFM scan of another RGO sensor site, the analysis of which is shown in Figure 20.

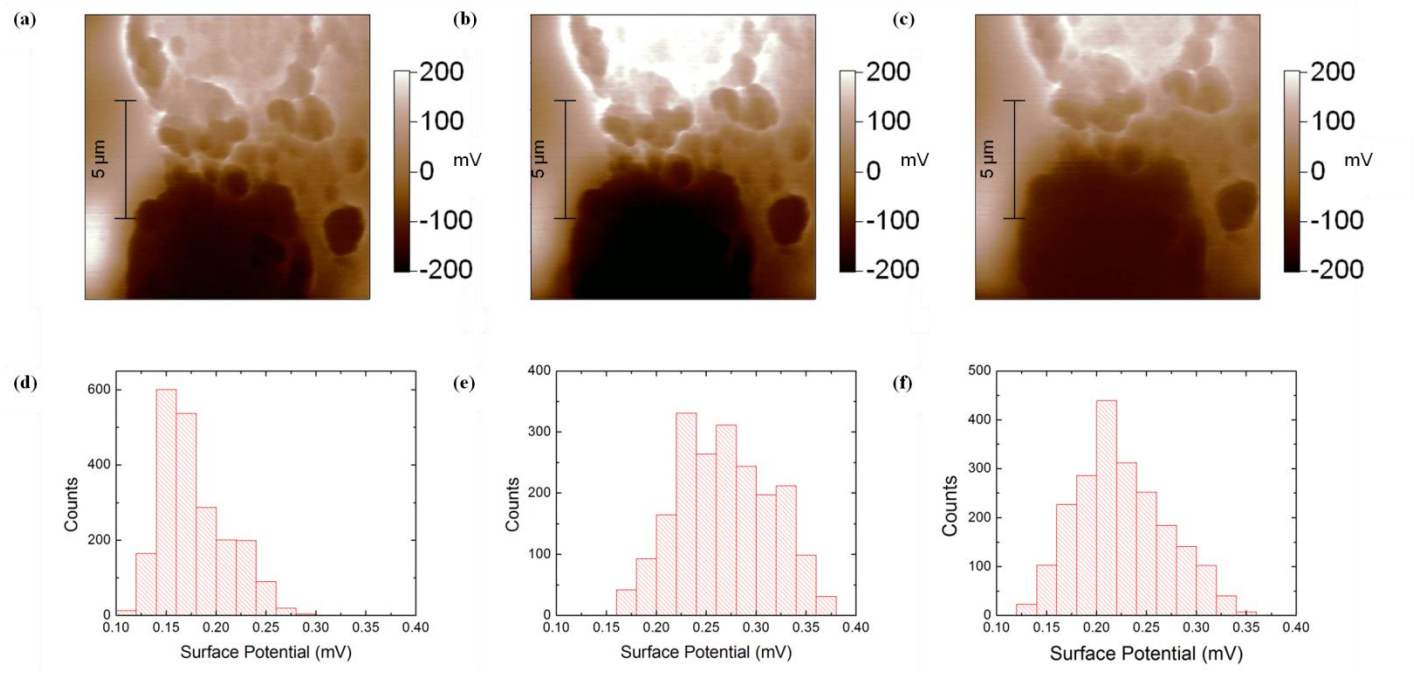

Figure 20: (a) SKPM potential map of nanosensor when it is unexposed. (b) SKPM potential map of nanosensor when it is exposed to acetone vapor. (c) SKPM potential map of nanosensor when it has had 30 minutes to relax since exposure to acetone. (d) Histogram of surface potential when unexposed with average value 173 mV and standard deviation 33 mV. (e) Histogram of surface potential when exposed to acetone with average value 265 mV and standard deviation 45 mV. (f) Histogram of surface potential when exposed to acetone with average value 237 mV and standard deviation 49 mV. The difference in charge distribution throughout the sample is shown graphically in (a,b,c) and also numerically in (d,e,f), demonstrating the sensitivity of the nanosensors' response to acetone exposure.

We combine the SKPM and transport data to quantify the amount of charge transferred due to chemical doping, as well as the contact resistance between the RGO and the Au electrodes. Assuming negligible change in the total sample capacitance *C* during acetone exposure we have that:

$$C = \frac{Q_{air}}{V_{air}} = \frac{Q_{air} + \Delta q_a}{V_{acetone}} \tag{13}$$

where $Q_{air} = e \cdot A \cdot n_{air}$ is the total electric charge when the device is exposed to air, and $\Delta q_a = e \cdot A \cdot \Delta n_a$ is the increase in the electric charge due to acetone exposure (here *A* is the sample surface area, while n_{air} and Δn_a represent the density of charge carriers in air, and the increase in the density of charge carriers, respectively). From this expression it follows that $\Delta q_a = Q_{air} \cdot \frac{V_{acetone} - V_{air}}{V_{air}}$, or in terms of charge carrier concentrations:

$$\frac{\Delta n_a}{n_{air}} = \frac{V_{acetone} - V_{air}}{V_{air}} \tag{14}$$

This latter relation shows that the percentage change in the charge carrier density due to doping is equal to the percentage change in the surface potential measured by KPM. Using the data displayed in Figure 18c and Figure 18d, we obtain $\frac{\Delta n_a}{n_{air}} = 0.4 \pm 0.2$.

We conclude that the surface charge density increased by about 40% (from the average of the two surface potential distributions shown in Figure 18). The absolute values for n_{air} and Δn_a can be estimated from the above result and the I_{SD}-V_G transport curves (Figure 17). Assuming a parallel plate model for the total capacitance *C*, we gather that, according to (15, 24):

$$\Delta n_a = \left(\frac{\varepsilon_0 \cdot \varepsilon}{t \cdot e} \right) \cdot \Delta V_{th} \tag{15}$$

where ε_0 and ε are the permittivity of the free space and of the Silicon Dioxide, and *t* = 200 nm is the thickness of the SiO_2 layer. With $\Delta V_{th} = 5V$ and $\Delta n_a / n_{air} \approx 0.4$, we obtain the following figures: $\Delta n_a \approx 5 \cdot 10^{11} cm^{-2}$ and $n_{air} \approx 1.2 \cdot 10^{12} cm^{-2}$. These are both values that are similar to typical charge carrier densities found for RGO and graphene-based sensors (3, 6, 17, 19).

Next, we combine the KPM results with the results obtained from the dynamic response (Figure 17) to quantify the contact resistance between the RGO and the electrode. The chemical doping model assumes that the surface coverage θ_{RGO} of analyte molecules on RGO (which is proportional to the available binding sites on RGO surface) determines the change in sample conductance and it is given by

$$\delta \cdot \theta_{RGO} = \frac{\Delta n_a}{n_{air}} \tag{16}$$

derived from (15, 30), where δ is a proportionality constant for a given analyte concentration and exposure time (15). We find that under these general assumptions, the change in the absolute value of the total resistance of the RGO platelets, $|\Delta R_{RGO}|$ due to gas exposure is

$$\frac{|\Delta R_{RGO}|}{R_{RGO}} = \frac{|\Delta R - \Delta R_C|}{R - R_C} = \frac{\delta \cdot \theta_{RGO}}{1 + \delta \cdot \theta_{RGO}} = B \tag{17}$$

where R_{RGO} is the resistance of the RGO platelets in air, *R* is the total resistance of the RGO device in air, R_C is the sample contact resistance in air, and ΔR and ΔR_C are the changes in the total sample resistance and the contact resistance due to analyte exposure, respectively.

This is similar to what was acquired in (15). Equation 17 shows that the relative change in the resistance of the RGO platelets is a constant (denoted as *B*) for given analyte concentration and exposure time. By combining equations 16 and 17 above and using our result from KPM measurements: $\Delta n_a / n_{air} \approx 0.4$ we obtain

$$B = \frac{\left(\frac{\Delta n_a}{n_{air}}\right)}{1+\left(\frac{\Delta n_a}{n_{air}}\right)} \approx 0.29$$

In addition, from the dynamic response data (shown in Figure 17), we have the following:

$$\frac{|\Delta R|}{R} \approx 0.25$$

Furthermore, our KPM data (Figure 18a-c) also show no significant change in the surface potential near the electrodes during acetone exposure, implying a negligible change in contact resistance upon doping: $\Delta R_C / R \approx 0$. This result is usually assumed in literature (15); however, to our knowledge, this is the first direct measurement which shows that the change in the sensor contact resistance is very small, during chemical doping. This is a non-trivial result demonstrating that that the sensing response is mainly due to charge transfer between RGO and analytes, and is not due to Schottky contacts or functional groups at the interface between the RGO and the electrodes. Combining this result with the results given by equations 13, 14 and 15 we conclude that the contact resistance between the RGO platelets and the sample electrode is negligible compared to the total sample resistance- that is,

$$\frac{R_C}{R} \approx 1 - \frac{1}{B} \cdot \left(\frac{|\Delta R|}{R}\right) \approx 0.14$$

Since $R = 287K\Omega$ and $|\Delta R| / R = 0.25$, we calculate that $R_C \approx 40K\Omega$. We emphasize that this result is obtained directly from measurements, by combining KPM and transport data. Thus the combination of KPM and transport/dynamic resistance data provides a general method for measuring the contribution of the contact resistance between the RGO sample and the metallic electrodes. This has important practical implications for building chemical sensors as the contact resistance could distort the sensitivity of the sensing device (15).

Finally, we note that similar results are obtained from the data on NH_3 sensing, thus demonstrating the consistency of the described combined KPM-transport method. Figure 20 shows the KPM image (Figure 20a) and surface potential distribution (Figure 20b) for the device exposed to NH_3. From the distribution of the surface potential we get the average value $V_{NH3} = (60 \pm 40) mV$, that is a negative shift with respect to $V_{air} = (178 \pm 31) mV$, consistent with a decrease in surface charge density. Combining this data with the dynamic response measurements, and following the same analysis as for acetone we obtain

$$\frac{|\Delta n_{NH3}|}{n_{air}} \approx 0.6$$

and negligible contact resistance, $R_C < 10K\Omega$. Therefore the KPM data allows us to estimate the ratio between the changes in carrier concentrations due to acetone vs. NH_3 doping:

$$\frac{\Delta n_a}{|\Delta n_{NH3}|} \approx \frac{0.4}{0.6} = 0.66$$

This result is in excellent agreement with the result given by the value of 1 - B, which computes to 1 - 0.29 = 0.71 (remembering of course that the value of B was obtained independently from the I_{SD}-V_G transport curves). Finally, by combining the KPM and transport data we obtain a level of doping (decrease in hole concentration) due to NH_3 exposure of: $|\Delta n_{NH3}| \approx 7 \cdot 10^{11} cm^{-2}$.

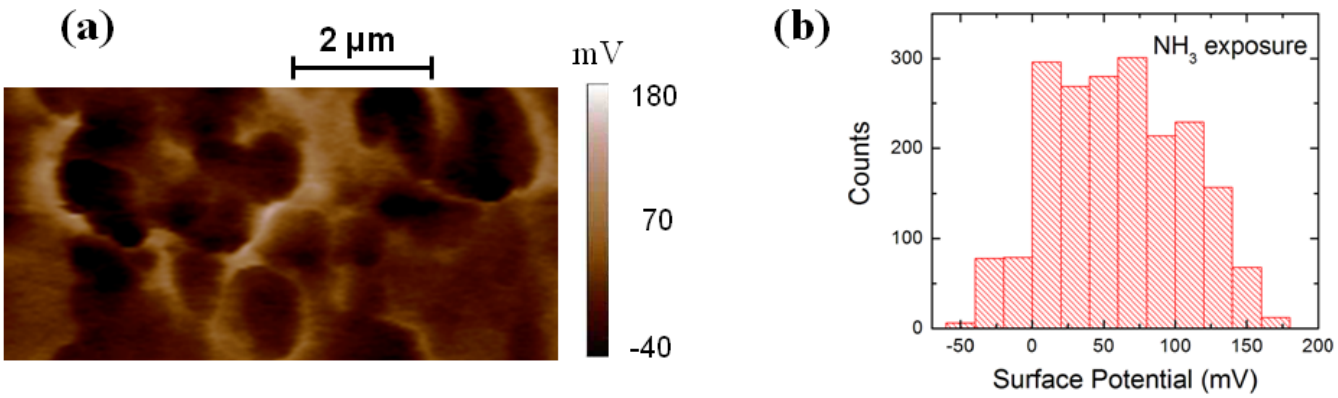

Figure 21: (a) KPM potential maps of an RGO sensor when exposed to ammonia. The image shows the variation in the surface potential due to gas exposure, and the active binding regions where chemical doping takes place. (b) Histogram of the surface potential for the image shown in (a). The average value/standard deviation for this distribution is $V_{NH3} = (60 \pm 40) mV$, consistent with a decrease in the carrier charge density due to adsorption of the electron-donor ammonia vapors.

3.3 Shifts in Fermi Energy

Further analysis of this doping effect involved using SKPM data to calculate the amount of electric charge transferred to the sensor by acetone doping. First, we note that in graphene the variation in carrier concentration is related to the shift in Fermi energy ΔE_F via (31,34):

$$\Delta n = \frac{2}{\hbar v_F} \cdot \sqrt{\frac{n}{\pi}} \Delta E_F \qquad (18)$$

where $v_F = 1.1 \cdot 10^8 cm/s$ is the Fermi velocity and $n = 10^{13} cm^{-2}$ is the concentration of charge carriers. We apply equation 2 to RGO by noting that, typically for this material, $v_F{}^{RGO} \approx 1/3 \cdot v_F{}^{graphene}$ and the carrier concentration is very close to that of graphene (19). With these values and by measuring $\Delta E_F = 50 meV$ given by SKPM analysis, we obtain the change in carrier concentration due to acetone exposure: $\Delta n \approx 0.5 \cdot 10^{13} cm^{-2}$.

We emphasize that this result is a direct consequence of SKPM data, and the general model of carrier concentration variation given by $\Delta n = \frac{2}{\hbar v_F} \cdot \sqrt{\frac{n}{\pi}} \Delta E_F$.

To further test this result, we use the measured change in carrier concentration given by $\Delta n \approx 0.5 \cdot 10^{13} cm^{-2}$ to calculate the change in sample resistance upon doping. We have that $\frac{R_{acetone}}{R_{air}} = \frac{n}{n + \Delta n}$, which gives a percentage change in the resistance upon exposure $\frac{|\Delta R|}{R_{air}} = \frac{\Delta n}{n + \Delta n} \approx 30\%$ (10). This result is in close agreement with the measured change in resistance from transport measurements as displayed in Figure 15b.

3.4 EFM measurements on RGO Sensors

EFM measurements were performed on one of the prior RGO sensors used for SKPM measurements (the same sensor as shown topographically in Figure 19). Figure 22 illustrates the difference between undoped and doped states of the RGO device.

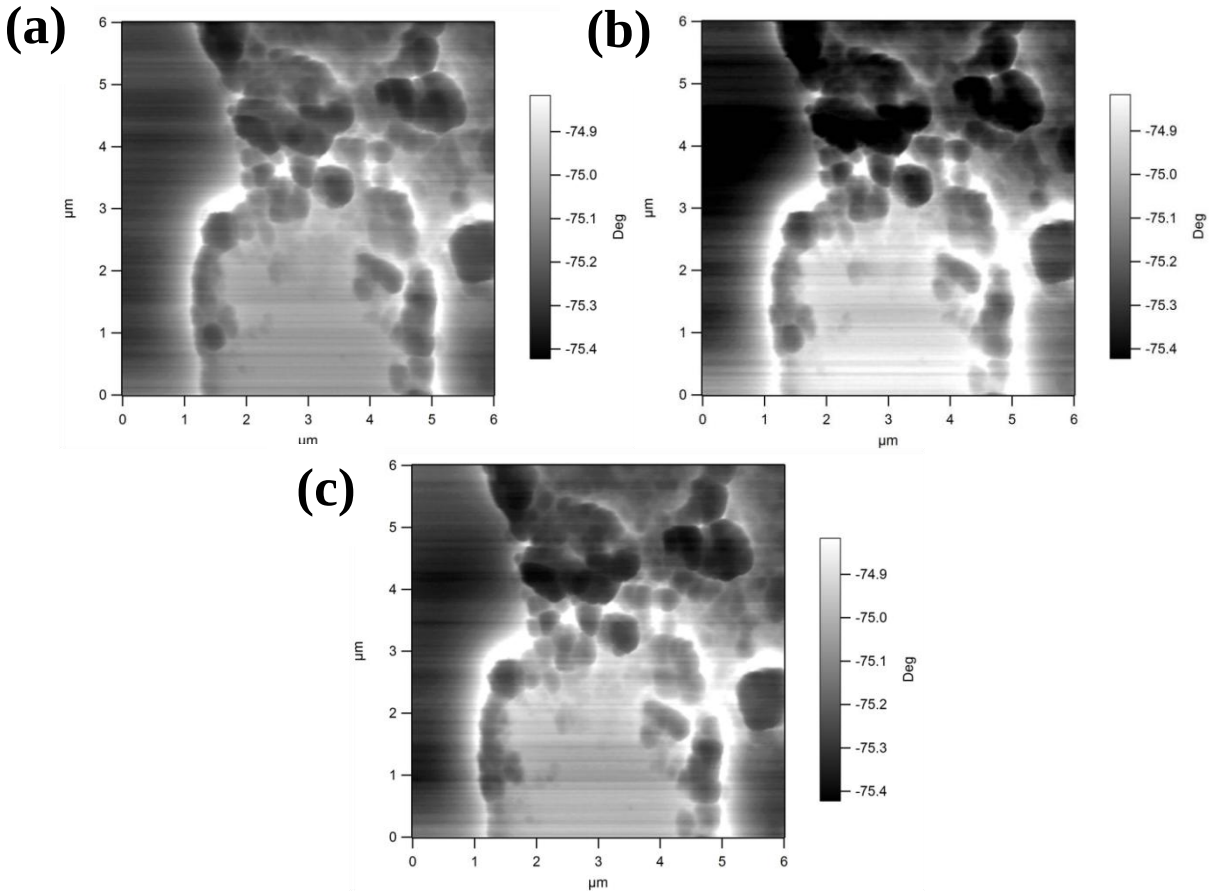

Figure 22: Shown are three consecutive EFM phase images taken of the same RGO sensor while exposed to air, acetone, and then air again. (a) Initially exposed to air, the phase map of the RGO sensor is displayed. The RMS value of the phase (taken from sampling the region between the electrodes) was 79.80^{o} with standard deviation 0.177^{o}. (b) Now, the sensor is exposed to acetone, resulting in a similar RMS value for the phase (75.12^{o}) but with larger distribution (standard deviation of 0.315^{o}). (c) Finally, after the RGO sensor was allowed to relax for 30 minutes, the sensor was allowed to relax after its exposure to acetone. The RMS value for the phase was 75.11^{o} with standard deviation 0.173^{o}.

From the figure above, it appeared that the mean value for the phase in the region between the electrodes varied only slightly between doped and undoped cases. However, it was also noted that the distribution of local phase measurements (and thus, local charge distributions) increased noticeably. This could mean that the depletion width of the FET-configured RGO sensor has grown as an effect of the chemical doping, thus causing an increase in the distribution of charges locally.

3.5 SIM Measurements on RGO Sensors

We performed SIM measurements on one of our RGO samples, with and without exposure to acetone. The results are shown in Figure 23b - j (spread over the next two pages). Certain regions of the amplitude and phase maps change between undoped and doped cases.

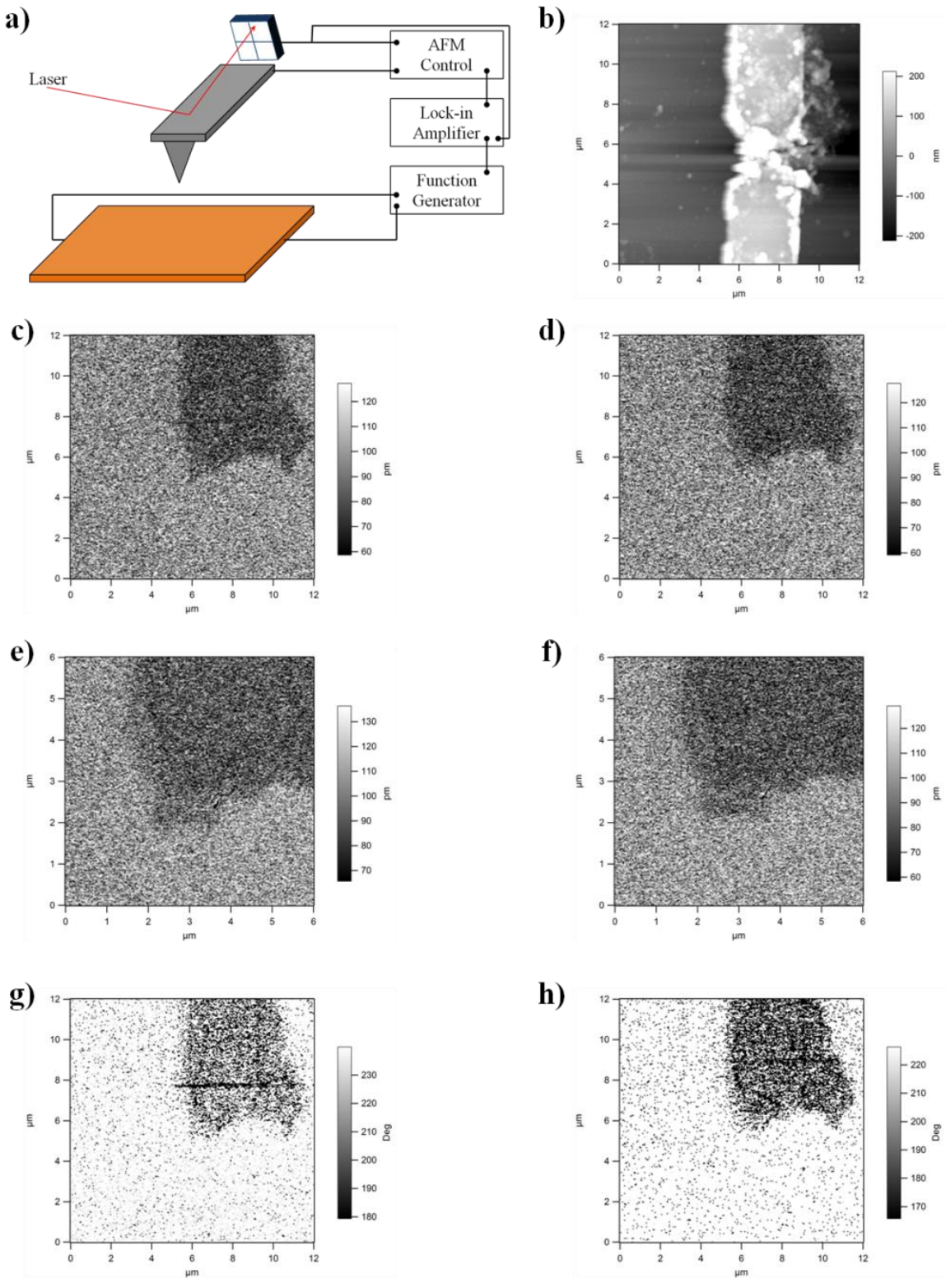
a)
Laser
AFM Control
Lock-in Amplifier
Function Generator
b)
c)
d)
e)
f)
g)
h)
µm
nm
pm
Deg

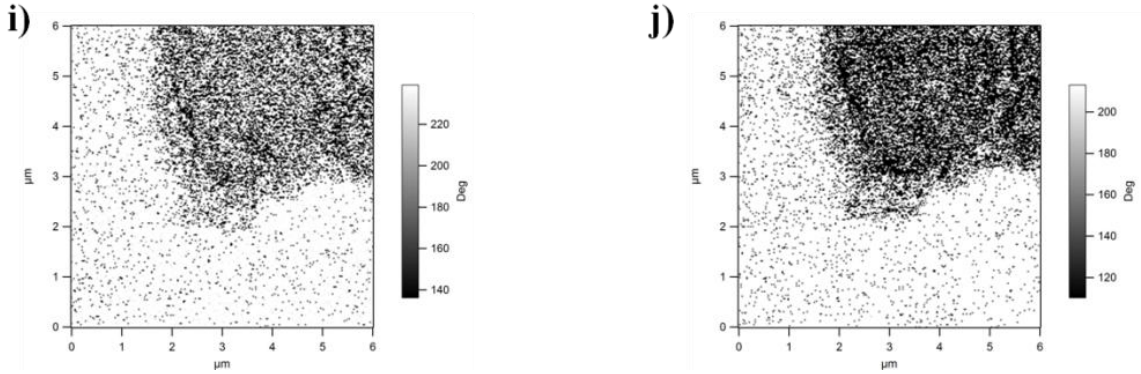

Figure 23: (a) Schematic of SIM concept. (b) Topography of RGO sample used for the SIM experiment. (c) Amplitude map of the same region using SIM using tip bias V_{tip} = 10V and sample bias V_{sample} = 1V (undoped case). (d) Same region and parameters, but doped. (e) This is a zoomed-in amplitude map (undoped case). (f) Same region, but doped. (g)-(j) Same scans as (c)-(f), only these are phase maps.

It seems that the signal-to-noise ratio is too low to be able to spot any clear differences between the doped and undoped cases for both amplitude and phase traces. However, close inspection seems to identify a few regions (with RGO platelets deposited between and to the side of the electrode) that have a shift in the mean amplitude and phase. For example, comparison between Figure 23c and Figure 23d show a few regions toward the center of each image where the amplitude experiences an upward shift. Also, the contrast between the two images, as viewed from the point of view of the top electrode, seems to increase. This increase is much more dramatic in the phase images when comparing Figure 23g, h and Figure 23i, j respectively.

4. Conclusions

We have used a combined Scanning Probe Microscopy technique to report high-resolution measurements of chemical doping effects in reduced graphene oxide-based gas sensors and, in doing so, have taken the first steps towards understanding the sensing mechanism exhibited by the RGO material. The sensing devices are fabricated by means of dielectrophoretic assembly of RGO platelets between gold electrodes, and show clear specificity and reversibility when exposed to acetone and ammonia. Kelvin Probe Microscopy, together with electronic transport measurements, provides us with the information that the doping occurs mainly within the RGO platelets with negligible contribution from contact resistance. We also calculate the amount of charge transferred to RGO due to chemical doping when the device is exposed to acetone and ammonia, and measure the contact resistance between the RGO and the metallic electrodes.

Our experimentation confirmed the sensors constructed from RGO assemblies displayed highly selective and reversible responses to certain measured analytes, as well as response and recovery times comparable to those of other devices (15). We used combined electronic transport and Kelvin Probe Microscopy measurements to quantify the amount of charge transferred to RGO due to chemical doping when the device is exposed to acetone and ammonia. We demonstrated that this method allows us to obtain high-resolution maps of the surface potential and local charge distribution both before and after chemical doping, to identify local gate-susceptible areas on the RGO surface, and to directly extract the contact resistance between the RGO and the metallic electrodes. Since the method presented is general, it is suggested that these results have important implications for fabricating graphene and other nanomaterial-based chemical sensors. We also measured localized charge distributions throughout the RGO surface with and without exposure to acetone vapor.

The gas sensing properties of these devices were first demonstrated and characterized using electrical transport measurements in the presence of gas. Acetone and ammonia vapors were delivered to the device from a reservoir of saturated vapors. The sensitivity, specificity, and reproducibility (as well as excitation and relaxation time) for these RGO sensors were characterized from these transport measurements.

Next, potential maps were taken of the RGO sensors using SKPM before and after exposure to acetone. The purpose of SKPM was to match the DC component of the cantilever potential to that of the surface, thereby recording the distribution of the surface potential along the sample surface.

Using results from both transport measurements and from literature, calculations for the variations in Fermi energy were conducted. These calculations serve to elucidate the source of physical contributions to the charge transportation throughout the material and the contributions of the molecular structure to its ability to sense organic vapors.

EFM measurements were also performed on the same RGO sensors as with the SKPM measurements. From these measurements, phase maps were used to identify regions within the RGO platelets that had the largest increase or decrease in charge concentration, thus allowing for the determination of regions that were most susceptible to analyte exposure. While the RGO sensors were exposed to acetone, it was noted that the distribution of local phase measurements (and thus, local charge distributions) increased noticeably. This could mean that the depletion width of the FET-configured RGO sensor has grown as an effect of the chemical doping, thus causing an increase in the distribution of charges locally.

Scanning Impedance Microscopy was employed in order to experiment with high-resolution techniques on the same RGO sensors. With similar motivation to use this technique as with EFM, Scanning Impedance Microscopy (SIM) measurements were performed with the expectation that the analysis method could be extended to study local chemical gating effects within smaller gate-susceptible regions of the RGO sample, and to correlate the local surface charge with surface functional groups on RGO. The goal was to utilize SIM in order to investigate whether or not this technique can provide us with higher resolution images and possibly even illuminate the locations of active sites within the

molecular structure of the RGO samples. At this point, the signal-to-noise ratio is too low to be able to spot any clear differences between the doped and undoped cases for both amplitude and phase traces, though close inspection seems to identify a few regions (with RGO platelets deposited between and to the side of the electrode) that have a shift in the mean amplitude and phase.

5. Future Developments

The transport and SKPM measurements have been utilized for several sensors over the course of many different experiments. However, calculations of the Fermi energy will need to be more in-depth in order to derive more accurate (and physically meaningful) values for the Fermi energy. Also, the techniques of EFM and SIM are still under development, as progress must be made in both improving the technique in order to acquire lower-noise measurements and in the interpretation of these measurements.

For more meaningful calculations of the Fermi energy, it is instructive to use as simple geometry for the FET configuration as possible (not like the geometry shown topographically in Figure 15a). This simplifies the model greatly and aids in the calculation (and our confidence in the calculation's implications) of the Fermi energy. Also, using clean and geometrically consistent arrangement for the RGO platelets is optimal. The fewer layers that scatter on top of each other, the better our confidence in the consistency of our measurements. Additionally, it has been suggested to try developing a patterning technique where the RGO is suspended from the Silicon substrate (in that each end of the region of patterned platelets will touch the top edge of each gold electrode). This may significantly improve resolution and decrease noise, thus improving measurements for the shift in Fermi energy.

The EFM measurements performed seem to have some significance, but it will take more measurements and a more tangible procedure (which will be achieved once we have a more comprehensible model of the RGO system) to improve this technique to a point where it will have convincing outcomes. The fact that the distribution of phase analyzed between the electrodes where the RGO platelets are deposited is an interesting observation (though far from conclusive), and our next step could be to investigate this phenomenon (or lack thereof).

Finally, the SIM technique needs to be better developed. This is a well-known, high-resolution technique that should not have such low signal-to-noise. Once experimental parameters are optimized and the technique is improved, it will be very interesting to see whether or not this high-resolution technique will be able to locate regions within the RGO assemblies that are susceptible to chemical doping due to significant charge transfer, possibly implying the existence of exposed binding sites for this type of sensing.

References

1. Novoselov KS, Geim AK, Morozov SV, Jiang D, Zhang Y, Dubonos SV, Grigorieva IV, and Firsov AA 2004 Electric field effect in atomically thin carbon films. *Science* **306** 666-9.
2. Geim AK and Novoselov KS 2007 The rise of graphene. *Nat Mater.* **6** 183-91.
3. Chen JH, Jang C, Xiao S, Ishigami M, and Fuhrer MS 2008 Intrinsic and extrinsic performance limits of graphene devices on SiO2. *Nat Nanotechnol.* **3** 206-9.
4. Zhang Y, Tan YW, Stormer HL, Kim P 2005 Experimental observation of the quantum Hall effect and Berry's phase in graphene. *Nature* **438** 201-4.
5. Lee C, Wei X, Kysar JW, and Hone J 2008 Measurement of the elastic properties and intrinsic strength of monolayer graphene. *Science* **321** 385-8.
6. Zhu Y, Murali S, Cai W, Li X, Suk JW, Potts JR, and Ruoff RS 2010 Graphene and graphene oxide: synthesis, properties, and applications. *Adv. Mater.* **22** 3906-24.
7. Schedin F, Geim AK, Morozov SV, Hill EW, Blake P, Katsnelson MI, and Novoselov KS 2007 Detection of individual gas molecules adsorbed on graphene. *Nat. Mater.* **6** 652-5.
8. Dan Y, Lu Y, Kybert NJ, Luo Z, and Johnson AT 2009 Intrinsic response of graphene vapor sensors. *Nano Lett.* **9** 1472-5.
9. Robinson JT, Perkins FK, Snow ES, Wei Z, and Sheehan PE 2008 Reduced graphene oxide molecular sensors. *Nano Lett.* **8** 3137-40.
10. Fowler JD, Allen MJ, Tung VC, Yang Y, Kaner RB, and Weiller BH 2009 Practical chemical sensors from chemically derived graphene. *ACS Nano* **3** 301-6.
11. Mao S, Lu G, Yu K, Bo Z, and Chen J 2010 Specific protein detection using thermally reduced graphene oxide sheet decorated with gold nanoparticle-antibody conjugates. *Adv. Mater.* **22** 3521-6.
12. Kim DJ, Sohn IY, Jung JH, Yoon OJ, Lee NE, and Park JS 2013 Reduced graphene oxide field-effect transistor for label-free femtomolar protein detection. *Biosens. Bioelectron.* **41** 621-6.
13. Ohno Y, Maehashi K, Yamashiro Y, and Matsumoto K 2009 Electrolyte-gated graphene field-effect transistors for detecting pH and protein adsorption. *Nano Lett* **9** 3318-22.
14. Mohanty N and Berry V 2008 Graphene-based single-bacterium resolution biodevice and DNA transistor: interfacing graphene derivatives with nanoscale and microscale biocomponents. *Nano Lett.* **8** 4469-76.
15. Lu G, Park S, Yu K, Ruoff RS, Ocola LE, Rosenmann D, and Chen J 2011 Toward practical gas sensing with highly reduced graphene oxide: a new signal processing method to circumvent run-to-run and device-to-device variations. *ACS Nano* **5** 1154-64.
16. Dua V, Surwade SP, Ammu S, Agnihotra SR, Jain S, Roberts KE, Park S, Ruoff RS, and Manohar SK 2010 All-organic vapor sensor using inkjet-printed reduced graphene oxide. *Angew. Chem. Int. Ed. Engl.* **49** 2154-7.
17. Lu Y, Goldsmith BR, Kybert NJ, and Johnson AT 2010 DNA-decorated graphene chemical sensors. *Appl. Phys. Lett.* **97** 083107.

18. Lu G, Ocola LE, and Chen J 2009 Reduced graphene oxide for room-temperature gas sensors. *Nanotechnology* **20** 445502.
19. Loh KP, Bao Q, Eda G, and Chhowalla M 2010 Graphene oxide as a chemically tunable platform for optical applications. *Nature Chem.* **2** 1015-24.
20. Wang S, Ang PK, Wang Z, Tang AL, Thong JT, and Loh KP 2010 High mobility, printable, and solution-processed graphene electronics. *Nano Lett.* **10** 92-8.
21. Stankovich S, Dikin DA, Piner RD, Kohlhaas KA, Kleinhammes A, Jia Y, Wu Y, Nguyen ST, and Ruoff RS 2007 Synthesis of graphene-based nanosheets via chemical reduction of exfoliated graphite oxide. *Carbon* **45** 1558-65.
22. Si Y and Samulski ET 2008 Synthesis of water soluble graphene. *Nano Lett.* **8** 1679-82.
23. MacNaughton S, Surwade S, Ammu S, Manohar S, and Sonkusale S Carbon nanotube and graphene based gas microsensors fabricaed by dielectrophoresis on silicon *IEEE SENSORS 2010 Conference 2010, 894-897*.
24. Jung I, Dikin DA, Piner RD, and Ruoff RS 2008 Tunable electrical conductivity of individual graphene oxide sheets reduced at "low" temperatures. *Nano Lett.* **8** 4283-7.
25. Gilje S, Han S, Wang M, Wang KL, and Kaner RB 2007 A chemical route to graphene for device applications. *Nano Lett.* 7 3394-8.
26. Staii C, Chen M, Gelperin A, and Johnson AT 2005 DNA-decorated carbon nanotubes for chemical sensing. *Nano Lett.* **5** 1774-8.
27. Melitz W, Shena J, Kummela AC, and Lee S 2011 Kelvin probe force microscopy and its application. *Surface Science Reports* **66** 1-27.
28. A.E. C, Fuhrer MS, Tedesco JL, Myers-Ward RL, Eddy CR, and Gaskill DK 2011 Kelvin probe microscopy and electric transport regime in graphene on SiC(0001) in the minimum conductance regime. *Appl. Phys. Lett.* **98** 243111.
29. Yu YJ, Zhao Y, Ryu S, Brus LE, Kim KS, and Kim P 2009 Tuning the graphene work function by electric field effect. *Nano Lett.* **9** 3430-4.
30. Lee CY and Strano MS 2005 Understanding the dynamics of signal transduction for adsorption of gases and vapors on carbon nanotube sensors. *Langmuir* **21** 5192-6.